JM PAPERS

Bubble shape oscillations in a turbulent environment

Aliénor Rivière[1]**, Kamel Abahri**[1] **and Stéphane Perrard**[1],†

[1]PMMH, CNRS, ESPCI Paris, Université PSL, Sorbonne Université, Université de Paris, 75005 Paris, France

We study single bubble deformation statistics in an homogeneous and isotropic turbulent flow by means of direct numerical simulations. We consider bubbles at low Weber number ($We < 3$) that have not been broken. We show that we can reproduce bubble deformations with a linear dynamics for each spherical harmonic mode. Inferring the coefficients of the linear model from the DNS data, we find that the natural frequency corresponds to the Rayleigh frequency, derived in a quiescent flow. However, the effective damping increases by a factor 7 compared with the quiescent case, at Taylor Reynolds number $Re_\lambda = 55$. Looking at the flow structure around the bubble, we argue that the enhanced damping originates from a thick boundary layer surrounding the bubble. We demonstrate that the effective forcing, originating from the turbulent flow forcing on the bubble surface, is independent of bubble deformability. Therefore, the interface deformations are only one-way coupled to the flow. From this model we conclude that bubbles break rather from turbulent fluctuations than from a resonant mechanism. Eventually, we investigate the pressure modes' statistics in the absence of bubbles and compare them with the effective forcing statistics. We show that both fields share the same probability distribution function, characterized by exponential tails, and a characteristic time scale corresponding to the eddy turnover time at the mode scale.

Key words: bubble dynamics, isotropic turbulence

1. Introduction

1.1. *Broad context*

Bubbly turbulent flows are widely used in industrial processes to enhance mass transfers and chemical reactions. Examples involve bubble column reactors (Risso [2018]) and emulsifiers (Håkansson [2019], [2021]) for instance. In geophysical contexts, bubbles are known to control aerosol productions at the ocean–atmosphere interface, while playing a major role in gas transfers (Deike [2022]). In both industrial and natural situations, the knowledge of the bubble size distribution and its temporal evolution is necessary to predict mass transfers across bubble interfaces. As a consequence, the study of bubble

† Email address for correspondence: stephane.perrard@espci.fr

breakup in turbulence has received considerable attention since the pioneering works of Kolmogorov (1949) and Hinze (1955). They predicted that, for bubbles of size lying within the inertial range of the turbulent cascade, the bubble dynamics and breakup are primarily controlled by the balance between inertial and capillary forces. This ratio defines the Weber number $We(d) = \rho U^2 d/\gamma$, where ρ is the liquid density, U a characteristic velocity, d the bubble volume equivalent diameter and γ the surface tension between gas and liquid. In turbulence, assuming bubbles break due to velocity fluctuations at their scale, Kolmogorov and Hinze postulated that the characteristic velocity U is the average velocity increment at the bubble scale $\langle \delta u^2(d) \rangle^{1/2}$. When kinetic and capillary forces balance we have $We(d_h) \approx 1 \approx We_c$, which defines a critical size, the Kolmogorov–Hinze scale, d_h, separating statistically stable bubbles ($d < d_h$) from unstable bubbles ($d > d_h$). In practice, the critical size (and the critical Weber number) are only defined in a statistical sense and might depend on the time spent by the bubble within the turbulent region (Vela-Martín & Avila 2022; Ni 2024).

However, the main physical mechanism leading to breakup remained to be understood. Sevik & Park (1973) proposed a resonant mechanism, in which a bubble breaks due to series of excitations at its natural frequency, while other authors argue that large fluctuations are necessary for a bubble to break (Lee, Erickson & Glasgow 1987; Luo & Svendsen 1996; Wang, Wang & Jin 2003). To address this question, several authors describe the bubble deformation dynamics, either with the help of a linear damped harmonic oscillator (Risso & Fabre 1998; Ravelet, Colin & Risso 2011; Masuk, Salibindla & Ni 2021*b*) on the bubble Rayleigh modes (Rayleigh 1879), or via a tensorial equation for the main bubble axis of deformations (Masuk *et al.* 2021*a*). The latter assumes that bubble shape is mostly ellipsoidal while the former allows any bubble shape and describes each mode dynamics.

More generally, bubble deformations in turbulence constitute one of the many examples of the interaction between a turbulent flow and a deformable object. From plant oscillations in the wind (De Langre 2008), to disk (Verhille 2022) and fibre deformations in water (Rosti *et al.* 2018; Brouzet *et al.* 2021), many studies have aimed at finding a reduced dynamics for the amplitude of the relevant spatial modes of deformations, in the form of a damped harmonic oscillator, randomly forced by turbulence. A usual approach is to model the coefficients of an ordinary differential equation, as well as the statistics of a random forcing term that accounts for the turbulent forcing. For bubbles, the models use the theoretical quiescent values for the coefficients of the bubble natural frequency and damping rate. Forcing statistics are modelled using the velocity increment statistics in single-phase turbulent flows (Risso & Fabre 1998; Ravelet *et al.* 2011; Masuk *et al.* 2021*b*). We followed this approach in a previous work (Perrard *et al.* 2021), to show that, in the limit of large *We*, the breakup time is controlled by the initial velocity statistics. Here, we propose to follow a different approach and to directly measure the coefficients of the model and the forcing statistics from the deformation statistics of bubbles in turbulence, by performing numerical simulations.

We first review the bubble oscillation dynamics in quiescent flows and its phenomenological extensions to turbulent flows.

1.2. *Bubble dynamics in quiescent flows*

Rayleigh (1879) investigated the oscillation dynamics of inviscid drops in vacuum and bubbles in a quiescent inviscid flow. In the linear limit of deformation, the local radius of a bubble (or a drop) can be decomposed into axisymmetric modes using the basis of Legendre functions, which are indexed by the integer $\ell \in [2, \infty]$. Rayleigh showed that the

amplitude of each mode ℓ follows an harmonic oscillator equation, with a characteristic natural frequency writing

$$(\omega_\ell^q)^2 = 8(\ell - 1)(\ell + 1)(\ell + 2)\frac{\gamma}{\rho d^3}, \tag{1.1}$$

for bubbles, with $f_\ell^q = \omega_\ell^q/(2\pi)$ the characteristic frequency, where the exponent $\cdot^q$ emphasizes that computations where made in a quiescent flow. Later on, Lamb (1932) extended this work to gas bubbles oscillating in a liquid of low kinematic viscosity, ν. He found that the bubbles' modes oscillate at the Rayleigh frequency with a damping rate λ_ℓ^q, which reads

$$\lambda_\ell^q = 8(\ell + 2)(2\ell + 1)\frac{\nu}{d^2}, \tag{1.2}$$

for bubbles of negligible inertia and viscosity. In three dimensions, the bubble shape can be decomposed into the real spherical harmonic base, $Y_\ell^m(\theta, \phi)$, indexed by $\ell \in [2, \infty]$ and m an integer ranging from $-\ell$ to ℓ, where θ and ϕ are the co-latitude and longitudinal angles in spherical coordinates. The axisymmetric modes of Rayleigh and Lamb correspond to $m = 0$. We denote the dimensionless amplitude of the modes in the spherical harmonic base by $x_{\ell,m}$. The dynamics found by Lamb (1932) and Rayleigh (1879) applies to each spherical harmonic mode amplitude $x_{\ell,m}$, so that they follow a damped harmonic oscillator equation with natural frequency ω_ℓ^q and damping rate λ_ℓ^q independent of m

$$\ddot{x}_{\ell,m} + \lambda_\ell^q \dot{x}_{\ell,m} + (\omega_\ell^q)^2 x_{\ell,m} = 0. \tag{1.3}$$

When time is made dimensionless using the natural frequency ω_ℓ^q, this equation reads

$$x''_{\ell,m} + p(\ell)Oh\, x'_{\ell,m} + x_{\ell,m} = 0, \tag{1.4}$$

where $p(\ell) = 2\sqrt{2}(\ell + 2)(2\ell + 1)/[(\ell - 1)(\ell + 1)(\ell + 2)]^{1/2}$ and $'$ stands for a derivative with respect to the dimensionless time $\omega_\ell^q t$. The Ohnesorge number $Oh = \mu/\sqrt{\rho\gamma d}$, with $\mu = \nu\rho$, compares viscous with capillary effects, and controls the quality factor $Q_\ell^q = \omega_\ell^q/\lambda_\ell^q \sim Oh^{-1}\ell^{-1/2}$ of the Lamb oscillations.

To estimate the damping rate of small oscillations, Lamb (1932) computed the velocity gradients of the irrotational inviscid velocity field. Doing so, he underestimated the dissipation rate, as shown later by Miller & Scriven (1968), as most of the dissipation takes place within the bubble boundary layer, even when viscosity is low. Another approach is given by the normal-mode analysis (Chandrasekhar 1959; Reid 1960; Chandrasekhar 2013), for the spherical harmonic modes. This theory predicts an evolution of the bubble natural frequency and damping rate with the Ohnesorge number. No explicit formulation can, however, be derived: one needs to solve a characteristic equation for each value of Oh. This approach correctly takes into account viscous effects but only holds at long times, presumably when oscillations have already been completely damped, and does not describe the transient dynamics. Miller & Scriven (1968) demonstrated that, in the limit of vanishing viscosity, the normal-mode solution converges to the irrotational one in the bubble case. For drops, the same demonstration has been done by Chandrasekhar (1959) and Reid (1960).

Later on, Prosperetti (1977, 1980) unified the two approaches by studying the initial-value problem of a drop or a bubble oscillating in an initially quiescent flow. He demonstrated that, regardless of the value of Oh, the damped harmonic oscillator dynamics of Lamb (1932) holds at short times compared with the viscous time scale,

$t \ll R_0^2/\nu$, where $R_0 = d/2$ is the bubble equivalent radius. On the other hand, the normal-mode description of Chandrasekhar (1959) holds at long times, $t \gg R_0^2/\nu$. At intermediate time scales, Prosperetti (1977, 1980) demonstrated that the dynamics is more complex due to the existence of a memory term in the equation of motion of the modes, which couples the dynamics with the past evolution.

1.3. *Bubble deformations in turbulence*

For a bubble immersed in a turbulent flow, additional dimensionless parameters may control the deformation. Let us consider a bubble of negligible inertia and viscosity, equivalent diameter d, immersed in a fluid of density ρ, dynamic viscosity μ, with surface tension γ. When the surrounding flow field is a homogeneous and isotropic turbulent flow, characterized by an energy dissipation rate ϵ, and an integral length scale L_{int}, the Buckingham Π theorem predicts that the dynamics is controlled by three dimensionless numbers. Choosing a set of dimensionless numbers which decouple viscous effects from capillary effects, we obtain that a generic measure of shape deformation δ can be written as

$$\frac{\delta}{d} = F\left(We(d), Re(d), \frac{d}{L_{int}}\right), \tag{1.5}$$

where F is a dimensionless function. The Weber number $We(d) = 2\rho\epsilon^{2/3}d^{5/3}/\gamma$ compares inertial and capillary forces at the bubble scale. The Reynolds number $Re(d) = \sqrt{2}\rho\epsilon^{1/3}d^{4/3}/\mu$ balances inertial and viscous forces at the bubble scale. Finally, the ratio d/L_{int} is the scale separation between the bubble scale and the integral length scale. Note that using ϵ and d we can define a characteristic velocity $U = \sqrt{2}(\epsilon d)^{1/3} = \langle \delta u^2(d)\rangle^{1/2}$, the velocity increment at the bubble scale in homogeneous and isotropic turbulence (Pope 2000). When the bubble size lies within the inertial range of the turbulent cascade, the surrounding flow is scale invariant and we expect the dynamics to be independent of d/L_{int}. The bubble dynamics will then be primarily controlled by the Weber number. In the presence of gravity g, one must also include the Bond number $Bo = \rho g d^2/\gamma$, comparing gravity with capillary effects. For simplicity, we will not consider gravity in this study. This assumption is valid for bubble diameters smaller than the capillary length $\sqrt{\gamma/(\rho g)} \sim 2$ mm. In practice, looking at the temporal evolution of bubble deformation, our model may describe shape oscillations slightly above the capillary length.

In this work we focus on bubbles which do not break, corresponding to a bubble size d within the inertial range of the turbulent cascade and $d < d_h$. For a typical turbulent flow with $\epsilon = 1$ m^2 s^{-3}, and $We_c \approx 3$, $d_h = (We_c\gamma/(2\rho\epsilon^{2/3}))^{3/5} \approx 8$ mm and $Re(d_h) \approx 2300$. Note that $Re(d_h) \sim \rho^{1/5}\gamma^{4/3}/(\epsilon^{1/5}\mu)$ decreases as ϵ increases for a given pair of liquid and gas. It is worth mentioning that, as a consequence, an increase of the Taylor Reynolds number induces more viscous effects at the Hinze scale.

In order to predict bubble breakup, Risso & Fabre (1998) introduced a forced linear damped oscillator equation to describe the dynamics of sub-Hinze bubbles. Observing that the average deformation increases linearly with We, up to the threshold for bubble breakup, they postulated that a linear dynamics would be valid to describe bubble deformations up to this point. They assumed that the deformed radius $R(t)$ evolves following

$$\ddot{R} + \lambda\dot{R} + \omega^2 R = F_{ex}(t), \tag{1.6}$$

where λ is a damping rate, ω a natural frequency and $F_{ex}(t)$ an instantaneous forcing from turbulence. Bubble deformations and breakup are mainly controlled by the second spherical harmonic modes $\ell = 2$, which correspond to oblate–prolate oscillation (Risso & Fabre 1998; Ravelet *et al.* 2011; Perrard *et al.* 2021). As a consequence, as a first guess, they used the Rayleigh natural frequency of mode 2, $\omega = \omega_2^q$, (1.1), and the Lamb damping rate $\lambda = \lambda_2^q$, (1.2), even though these values only hold in a quiescent irrotational flow. Then, following the original idea from Kolmogorov (1949) and Hinze (1955), they assumed that the turbulent forcing from turbulence scales as the square of the instantaneous velocity increment at the bubble scale $\delta u(d, t)^2$, leading to a forcing $F_{ex}(t) = Kd^{-1}\delta u(d, t)^2$ from dimensional analysis, where K is a numerical constant of order 1. Doing so, they assumed that the presence of the bubble does not strongly affect the flow properties, so that the flow statistics correspond to the single fluid case. Expressing length in units of d, and time in units of $1/\omega_2^q$, (1.6) is now written as

$$r'' + 20\sqrt{2/3}\,Oh\,r' + r = \tilde{K}We(t), \tag{1.7}$$

where $\tilde{K}$ is also a numerical constant and $We(t) = 2\rho\delta u(d, t)^2 d/\gamma$ is the instantaneous bubble Weber number. This model is essentially the same as (1.4), with an additional random forcing term. This equation has been widely used for bubble (Ravelet *et al.* 2011; Lalanne, Masbernat & Risso 2019; Masuk *et al.* 2021*a*,*b*) and drop (Galinat *et al.* 2007; Maniero *et al.* 2012; Håkansson 2021; Roa *et al.* 2023) oscillations in turbulence with adequate expressions of the damping rate and natural frequency.

However, there is no guarantee that the bubble natural frequency and damping rate remain unchanged compared with the quiescent case. They may *a priori* depend on both *Re* and *We*. Indeed, surrounding flows are known to modify the natural frequency and the damping rate. For instance, for bubbles in a uniaxial inviscid straining flow, Kang & Leal (1988) showed that the flow couples modes $\ell = 2$ and 4, inducing a reduction linear in *We*, of the mode $\ell = 2$ natural frequency at linear order. Rivière *et al.* (2023) investigated numerically the deformation dynamics of bubbles in a uniaxial straining flow at large but finite Reynolds number. Together with the linear *We*-dependency, they reported an additional *Re*-dependency of the natural frequency of mode $\ell = 2$.

1.4. *Outline of the present work: inferring the bubble deformation dynamics from data*

In this paper, following Risso & Fabre (1998), we assume a linear damped oscillator equation with a stochastic forcing for the oscillations of each mode of bubble deformation. However, we do not presume either the values of the coefficients of (1.6) or the form of the forcing. Instead, we directly measure, from the deformation dynamics, the effective natural frequency and damping rate and compare them with the quiescent values. We then deduce the statistical properties of the effective forcing. Looking for a reduced model of the effective forcing, we compare its statistics with the pressure field evaluated in a single-phase flow, on a sphere. Eventually, we investigate the flow structure around the bubble and the local dissipation rate, to discuss the origin of the damping of bubble oscillations in turbulent flows.

2. Bubble deformations in homogeneous and isotropic turbulent flow

2.1. *Numerical set-up: direct numerical simulation of a single bubble in homogeneous and isotropic turbulent flow*

We perform direct numerical simulations of an incompressible gas bubble immersed in a homogeneous and isotropic turbulent flow of an incompressible liquid, using the

We	2.9	2	1.43	1	0.71	0.46	0.36	0.27
N	5	5	3	3	5	3	3	5
$T_{tot}/t_c(d)$	62	126	94	94	156	94	84	94

Table 1. Number of simulations and total simulated time per value of the Weber number.

open-source software Basilisk (http://basilisk.fr) (Popinet 2003, 2009; Abu-Al-Saud, Popinet & Tchelepi 2018). Density and dynamic viscosity ratios are set to 850 and 25, respectively, close to water–air ratios (830 and 58 respectively). The simulation goes in two steps. We first create a homogeneous isotropic turbulent flow by solving the one-phase incompressible Navier–Stokes equations with an additional forcing term proportional to the velocity (Rosales & Meneveau 2005). After a transient regime, the flow reaches a statistically stationary homogeneous and isotropic turbulent state. The turbulent fluctuations are characterized by the Taylor Reynolds number Re_λ, defined at the correlation length of the velocity gradients, namely the Taylor micro-scale $\lambda_T = \sqrt{15\nu/\epsilon}\, u_{rms}$ Pope (2000), where u_{rms} is the root mean square of the velocity. The Taylor Reynolds number of the flow is $Re_\lambda = u_{rms}\lambda_T/\nu = 55$. In physical units, assuming $\epsilon = 1$ m^2 s^{-3}, in water, we would have $u_{rms} = 0.12$ m s^{-1} and $\lambda_T = 0.46$ mm. We then extract snapshots of the flow and use them as flow initial conditions for bubble injection. At the bubble scale, flow structures are correlated on a typical time scale $t_c(d) = \epsilon^{-1/3} d^{2/3}$, called the eddy turnover time. To make sure the initial conditions are independent, we take flow snapshots separated by at least $6\,t_c$. The spherical bubble is injected at the centre of the simulation box by changing locally the density and viscosity. The bubble size is chosen so that it lies within the inertial range of the turbulent cascade where the flow is scale invariant. The bubble diameter to box length ratio is 0.13. During this second stage, forcing is maintained to sustain turbulence, but only in the liquid phase to guarantee that bubble deformations only come from the fluid forcing. In both steps, we use adaptive mesh grid refinement in order to save computational time while resolving all the physical length scales of the problem. The minimum grid size corresponds to 34 points per bubble radius. Details of the numerical set-up as well as a convergence study can be found in Rivière *et al.* (2021).

In this study we keep the Taylor Reynolds number constant and we vary the bubble Weber number by changing the value of the surface tension coefficient. The bubble Reynolds number is $Re(d) = 124$. Assuming $\epsilon = 1$ m^2 s^{-3}, this Reynolds would correspond to a bubble of size $d = 0.9$ mm. We explore eight values of *We* ranging from $We_c \approx 3$ to $0.1 We_c$. For each Weber number, we run between 3 and 5 simulations. Except when the bubble breaks (at $We = 2.9$), we run every simulation for at least $20\,t_c$, so that the total time per ensemble is approximately $100\,t_c$. Table 1 summarizes the exact number of simulations and total computational time per Weber number we perform.

2.2. *Modes of deformations*

To quantify bubble deformations, we decompose the local bubble radius R into the real spherical harmonic base $Y_\ell^m(\theta, \phi)$, where ℓ and m are the principal and secondary numbers
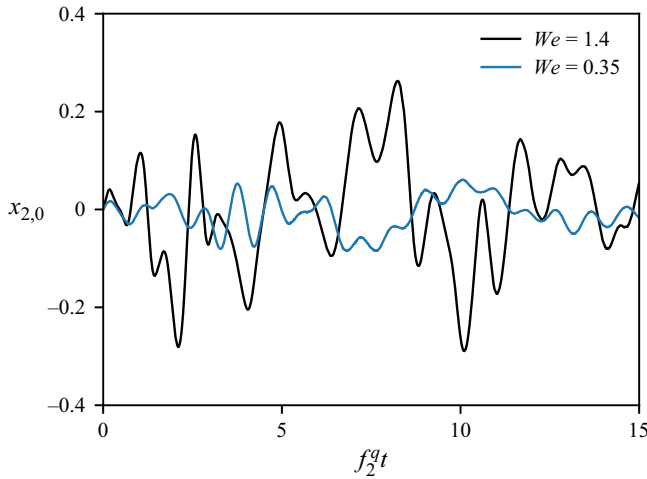
Figure 1. Typical temporal evolution for the mode $(2, 0)$ at two different Weber numbers. Time is made dimensionless using the Rayleigh frequency f_2^q. Modes exhibit random oscillations, with an amplitude that is increasing with *We*.

respectively, and θ and ϕ the co-latitude and longitude,

$$R(\theta, \phi, t) = R_0 \left[1 + \sum_{\ell=2}^{\infty} \sum_{m=-\ell}^{\ell} x_{\ell,m}(t) Y_\ell^m(\theta, \phi) \right], \tag{2.1}$$

and we track the modes' amplitude $x_{\ell,m}$ over time. Bubble shape is described in the bubble frame of reference so that all harmonics $\ell = 1$, corresponding to bubble translation, are null by definition. Numerically, the bubble centre is determined at each time step recursively by moving the frame origin to minimize the amplitudes of all modes $\ell = 1$. The recursion stops when the centre displacement between two steps is less than $2.5 \times 10^{-6} R_0$. This condition ensures that $|x_{1,m}| < 4 \times 10^{-6}$ for all values of m. Note that the spherical harmonic decomposition holds as long as the local radius R is mono-valued. The procedure to compute the spherical harmonics is described in detail in Perrard *et al.* (2021).

Figure 1 shows two typical temporal evolutions for the mode $(\ell, m) = (2, 0)$, at two different Weber numbers. Time is made dimensionless using the Rayleigh frequency f_2^q. For both *We*, we observe random oscillations around zero and the predominance of the bubble resonant frequency f_2^q. The amplitude of the oscillations increases with *We*.

Since we do not prescribe any special orientation relative to the bubble shape, all modes with the same principal number ℓ are statistically equivalent. Indeed, one can verify that a rotation of a mode can be expressed as a linear combination of all the other modes with the same principal number. As a consequence, we omit m in what follows. For instance, $x_\ell(t)$ represents a typical temporal evolution of one of the modes ℓ. In addition, assuming that $x_{\ell,m}$ are independent, the ensemble averaging operation $\langle \cdot \rangle$ is computed over different simulations and over the m values for a given ℓ. Roa *et al.* (2023) used a reference frame dynamically oriented with the bubble principal axis of deformations. In practice, their reference frame maximizes the amplitude of mode $(2, 0)$, such that the differential elongation can be studied as the invariance by rotation is broken.

3. Determination of the reduced dynamics

3.1. *Model: a stochastic linear oscillator*

Following Risso & Fabre (1998), we introduce a linear stochastic model to describe each mode's dynamics

$$\ddot{x}_\ell + \Lambda_\ell(We)\dot{x}_\ell + \Omega_\ell(We)^2 x_\ell = \mathcal{T}_\ell(We, t), \tag{3.1}$$

where Λ_ℓ and Ω_ℓ are the damping rate and natural frequency, respectively, and $\mathcal{T}_\ell$ is a random variable which models the turbulent forcing. In this section, we aim at measuring Λ_ℓ, Ω_ℓ and the statistical properties of $\mathcal{T}_\ell$ from the deformation dynamics. Note that Λ_ℓ, Ω_ℓ and $\mathcal{T}_\ell$ may also depend, in general, on the Reynolds number at the bubble scale. However, here, we keep the bubble Reynolds number fixed and investigate the dependency of Ω_ℓ, Λ_ℓ and $\mathcal{T}_\ell$ on the Weber number *We*. Conversely to what other authors have done, time is made dimensionless using the eddy turnover time at the bubble scale $t_c(d) = \epsilon^{-1/3} d^{2/3}$ and, from now on, $\dot{}$ denotes derivatives with respect to this dimensionless time. This choice avoids *a priori* the need to have a forcing term depending on bubble properties such as surface tension. It decorrelates the turbulent forcing (right-hand side), from the bubble response (the left-hand side). In these units, the Rayleigh frequency and the Lamb damping rate write $(\Omega_\ell^q)^2 = 16(\ell - 1)(\ell + 1)(\ell + 2)/We$ and $\Lambda_\ell^q = 8\sqrt{2}(\ell + 2)(2\ell + 1)Re(d)^{-1}$, respectively. Note that, in this study, we have not varied the eddy turnover time. When the bubble size lies within the inertial range of the turbulent cascade its dynamics is primarily controlled by inertial effects, and the parameters may not depend explicitly on the bubble Reynolds number, as long as $Re(d) \gg 1$.

In order to measure the coefficients and the force statistics of (3.1), we make the following assumptions:

(H1) The modes' dynamics is linear and uncoupled, which is valid for $x_\ell \ll 1$, corresponding to $We \ll 1$.
(H2) The bubble deformation is one way-coupled to the flow. This hypothesis is discussed in § 3.5.
(H3) The forcing $\mathcal{T}_\ell$ is statistically stationary.
(H4) The damping rate and the natural frequency do not depend on time.

From hypothesis (H2) the effective $\mathcal{T}_\ell$, in units of the eddy turnover time, is independent of *We*. From hypothesis (H3), the effective forcing is completely determined by its auto-correlation function (or equivalently its spectrum), and its probability distribution function (p.d.f.).

Under these hypotheses, in the next sections, we will show that

(i) The natural frequency is not modified by the presence of the flow: $\Omega_\ell = \Omega_\ell^q$.
(ii) There is an effective viscosity, driven by turbulence, so that $\Lambda_\ell = 0.6(\ell + 2)(2\ell + 1)$ for $Re(d) = 124$.

Combining (i), (ii) and (3.1) we will deduce the statistical properties of the forcing $\mathcal{T}_\ell$.

3.2. *Frequency response of the oscillator – amplitude of the Fourier transform*

To rationalize the qualitative observations of figure 1 and identify the angular frequency Ω_ℓ, we investigate the frequency response of the bubble. To do so, we compute the
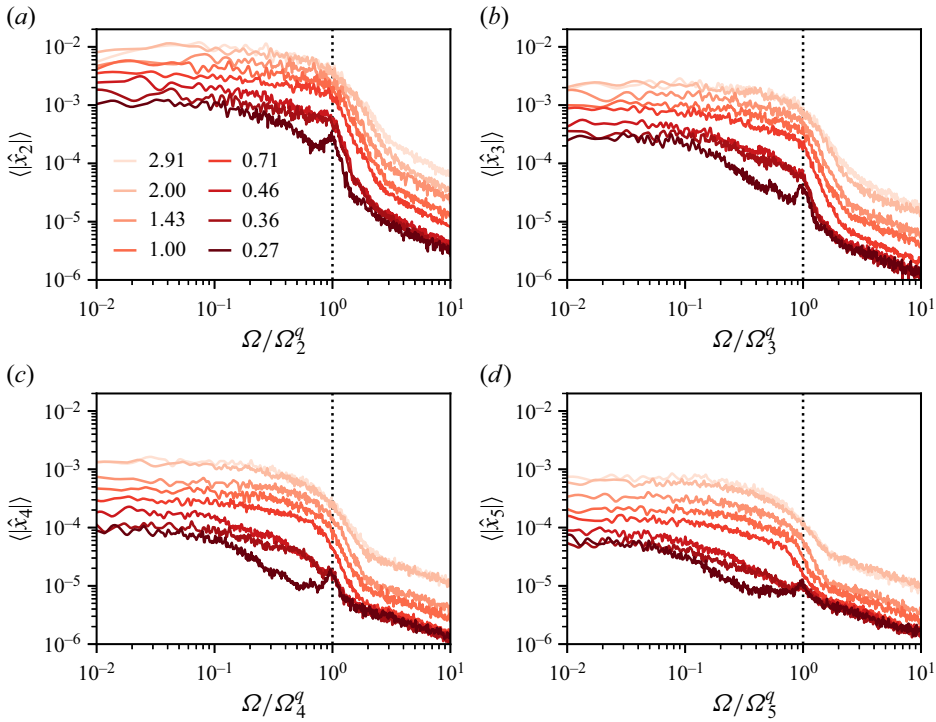
Figure 2. Amplitude of the modes' Fourier transform for all *We* as a function of the frequency normalized by the corresponding Rayleigh frequency. The Weber number value is colour coded.

temporal Fourier transform, $\hat{x}_\ell$ of x_ℓ for all ℓ and *We*

$$\hat{x}_\ell(\Omega) = \frac{1}{T}\int_0^T x(t)e^{-i\Omega t}dt, \tag{3.2}$$

where $\hat{x}_\ell$ is also a random variable, T is the duration of the time signal and Ω is the angular frequency. Similarly, we introduce $\hat{\mathcal{T}}_\ell$, the Fourier transform of the effective forcing

$$\hat{\mathcal{T}}_\ell(\Omega) = \frac{1}{T}\int_0^T \mathcal{T}(t)e^{-i\Omega t}dt. \tag{3.3}$$

Figure 2 shows the ensemble average $\langle|\hat{x}_\ell|\rangle$ as a function of the angular frequency Ω, normalized by the corresponding Rayleigh natural frequency Ω_ℓ^q.

For $\Omega < \Omega_\ell^q$, for every *We*, $\langle|\hat{x}_\ell|\rangle$ is approximately constant. The low-frequency dynamics is similar to that of a white noise.

At $\Omega = \Omega_\ell^q$ (back dotted line), for *We* ≤ 0.46 we observe a peak that resembles the resonant response of an oscillator at its natural frequency. This peak does not exist for larger values of *We*. Nevertheless, for every ℓ, we observe a transition at this very frequency.

For $\Omega > \Omega_\ell^q$, at all *We*, we report a sharp power-law decay, following at least $(\Omega/\Omega_\ell^q)^{-4}$.

Finally, for $\Omega > 3\Omega_\ell^q$, the spectrum amplitude is below the noise level. Note that this part also corresponds to the end of the inertial range.

Dimensional measurements of bubble deformation dynamics were performed by Ravelet *et al.* (2011) in the context of bubbles rising in turbulence. They measured the temporal spectrum of the horizontal bubble main axis, a proxy for the amplitude of the second Rayleigh mode. The overall shape of their power spectrum was similar: weak variation for $\Omega < \Omega_\ell^q$, no resonance at Ω_2^q and a strong decay for $\Omega > \Omega_\ell^q$. In the absence of gravity, Risso & Fabre (1998) also reported a transition at Ω_2^q, with a rapid decay for $\Omega > \Omega_\ell^q$ of the projected area spectrum.

The cutoff frequency being Ω_ℓ^q for all considered cases, we deduce that the bubble natural frequency in turbulence, Ω_ℓ of (3.1), is not modified by the presence of the surrounding turbulent flow and that

$$\Omega_\ell = \Omega_\ell^q = 4 \left[\frac{(\ell - 1)(\ell + 1)(\ell + 2)}{We} \right]^{1/2}. \tag{3.4}$$

It is surprising that the bubble natural frequency remains unchanged. Indeed, Prosperetti (1980) showed, for a bubble in an initially quiescent flow, that viscous effects induce an additional memory term in the bubble dynamics. This memory term can be modelled by an effective natural frequency and damping term. The surrounding flow field can also modify the natural frequency. In a uniaxial straining flow for instance, Kang & Leal (1988) demonstrated that a coupling between modes $\ell = 2$ and $\ell = 4$ decreases the mode 2 natural frequency at linear order, with a corrective term linear in *We*. We hypothesize that the stochastic nature of turbulence cancels, on average, these contributions. In the following, we use the theoretical expression of Ω_ℓ^q, for the bubble natural frequency, Ω_ℓ.

3.3. *Zero frequency limit and We-dependency of the forcing*

In this section, we investigate the zero frequency limit, and discuss the consequence for the *We*-dependency of the forcing. By computing the Fourier transform of (3.1), combined with (3.4), we obtain an expression linking $\hat{x}_\ell$ and $\hat{\mathcal{T}}_\ell$

$$|\hat{x}_\ell|(We, \Omega) = \frac{|\hat{\mathcal{T}}_\ell|(We, \Omega)}{\sqrt{(\Omega^2 - \Omega_\ell^q(We)^2)^2 + \Lambda_\ell(We)^2 \Omega^2}}. \tag{3.5}$$

The spectral behaviour of each x_ℓ is a combination of the forcing spectrum $\hat{\mathcal{T}}_\ell$ and the bubble response. In the limit case $\Omega = 0$, using the expression of the bubble natural frequency (3.4), we have

$$|\hat{x}_\ell|(We, 0) = \frac{|\hat{\mathcal{T}}_\ell|(We, 0)}{\Omega_\ell^q(We)^2} = \frac{We}{16(\ell - 1)(\ell + 1)(\ell + 2)} |\hat{\mathcal{T}}_\ell|(We, 0). \tag{3.6}$$

We can use this expression to investigate the *We*-dependency and ℓ-dependency of $\hat{\mathcal{T}}_\ell$ at $\Omega = 0$. We extract $\langle |\hat{x}_\ell| \rangle(We, 0)$ by averaging $\langle |\hat{x}_\ell| \rangle(We, \Omega)$ over the range $5 \times 10^{-3} < \Omega/\Omega_\ell^q < 10^{-1}$ where the spectrum is constant.

Figure 3(*a*) shows $\langle |\hat{x}_\ell| \rangle(We, 0)$ as a function of *We*. Solid lines of slope 1 are superimposed, showing that $\langle |\hat{x}_\ell| \rangle(We, 0)$ increases linearly with *We* for $\ell < 4$, up to $We = 2.9 \approx We_c$, when nonlinear effects start to be important. For $\ell \geq 4$, the increase is faster than linear. This effect might originate from nonlinear coupling with lower-order modes. It follows from (3.6) that $\langle |\hat{\mathcal{T}}_\ell| \rangle(We, 0)$ is independent of *We* for $\ell < 4$, the most energetic modes. This result justifies that the effective forcing from turbulence does not depend on
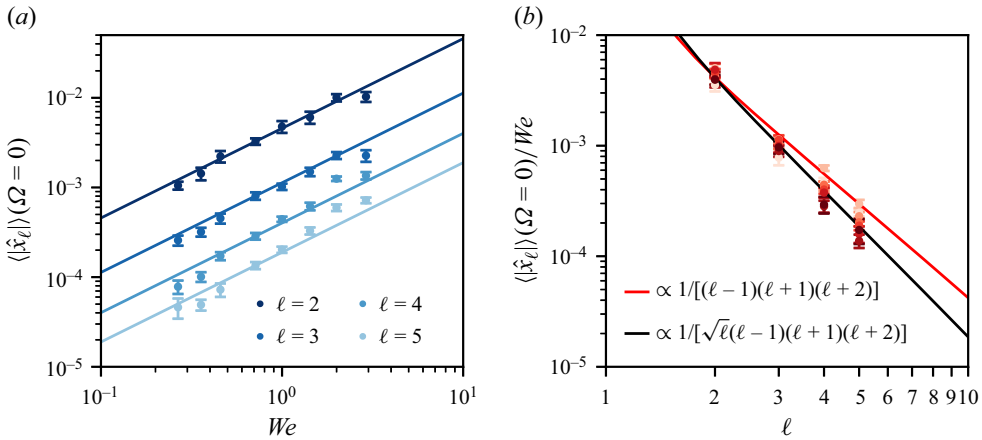
Figure 3. (*a*) Zero frequency limit of the modes' Fourier transform as a function of *We* for all ℓ. For comparison, solid lines have slope 1 and would represent $\langle|\hat{x}_\ell|\rangle(\Omega = 0) \propto We$. Error bars are estimated using the standard deviation of the spectrum value for $5 \times 10^{-3} < \Omega/\Omega_\ell^q < 10^{-1}$. (*b*) Compensated limit $\langle|\hat{x}_\ell|\rangle(\Omega = 0)/We$, as a function of ℓ. Colours encode *We* (see figure 2). Assuming $\mathcal{T}_\ell$ independent of ℓ gives the scaling plotted in red. Assuming $|\mathcal{T}_\ell| \sim 1/\sqrt{\ell}$ gives the scaling plotted in black.

the bubble deformability at low frequency. The modification of the flow induced by bubble oscillations does not impinge back on the bubble dynamics. A similar phenomenon has been observed for drops by Vela-Martín & Avila (2021). They investigated the interfacial stress generated by eddies depending on their distance from the interface. They concluded that eddies further that $0.2d$ from the drop interface (outer eddies) generate most of the stress. They reported that these contributions are, in addition, independent of *We*, as these eddies are too far from the interface to be affected by drop deformations. We can assume that a similar mechanism may hold also for the bubble dynamics so that $\hat{\mathcal{T}}_\ell$ does not depend on *We* either, at least for $\ell < 4$. These results justify hypothesis (H2) at low frequency, and we assume that (H2) holds for all frequencies. From now on, we therefore assume that $\mathcal{T}_\ell$ does not depend on *We*. This hypothesis will be further validated and tested in § 3.5. The zero frequency limit also depends on the mode order ℓ. Figure 3(*b*) shows the compensated spectrum limit $\langle|\hat{x}_\ell|\rangle(\Omega = 0)/We$ as a function of ℓ. We find that the zero frequency limit decreases slightly faster than $(\Omega_\ell^q)^{-2} \sim [(\ell - 1)(\ell + 1)(\ell + 2)]^{-1}$ of (3.6) (red line). It suggests that $|\hat{\mathcal{T}}_\ell|$ weakly decreases with ℓ, with $|\hat{\mathcal{T}}_\ell| \sim 1/\sqrt{\ell}$. Higher-order modes are associated with smaller scales that are less energetic. However, the direct investigation of pressure modes in § 5.2 showed a faster decrease of the mode energy with ℓ. The high-order modes $\ell \geq 3$ may also be indirectly forced from nonlinear coupling, with mode 2 changing the ℓ-dependency of the forcing.

3.4. *Determination of the effective damping factor: additional dissipation due to turbulence*

In this section, we present a method to compute the damping factor Λ_ℓ of (3.1) from the numerical data.

Let $\hat{x}_a$ and $\hat{x}_b$ be the Fourier transform $\hat{x}_\ell$ of the same mode ℓ for two Weber numbers We_a and We_b. For simplicity, here, we denote Ω_a and Λ_a, the natural frequency and

damping rate associated with We_a at this ℓ. Under hypothesis (H2), the ratio R_{ab}

$$R_{ab}(\Omega) = \left(\frac{\langle|\hat{x}_a|\rangle}{\langle|\hat{x}_b|\rangle}\right)^2 = \frac{(\Omega^2 - \Omega_b^2)^2 + \Lambda_b^2\Omega^2}{(\Omega^2 - \Omega_a^2)^2 + \Lambda_a^2\Omega^2} \tag{3.7}$$

is independent of $\hat{T}_\ell$.

Since the two natural frequencies Ω_a and Ω_b are known (3.4), one can estimate the two damping factors, Λ_a and Λ_b, using $R_{ab}(\Omega_a)$ and $R_{ab}(\Omega_b)$, the ratios at the two natural frequencies

$$R_{ab}(\Omega_a) = \frac{(\Omega_a^2 - \Omega_b^2)^2 + \Lambda_b^2\Omega_a^2}{\Lambda_a^2\Omega_a^2} \tag{3.8}$$

$$R_{ab}(\Omega_b) = \frac{\Lambda_b^2\Omega_b^2}{(\Omega_a^2 - \Omega_b^2)^2 + \Lambda_a^2\Omega_b^2}, \tag{3.9}$$

by solving this two-equation system. In practice, we measure R_{ab} at Ω_a and Ω_b using the Fourier amplitude shown in figure 2 and compute the corresponding values Λ_a and Λ_b. We repeat the procedure for all pairs We_a and We_b of Weber numbers. Note that an optimization of Λ_a and Λ_b on the whole range of frequencies was less reliable. The signal over noise ratio is optimal near the resonance, and decreases both at high and low frequencies. Indeed, high frequencies, which are the more noisy, then dominate the optimization procedure.

Figure 4(*a*) illustrates the computation of Λ_ℓ. The ratio $R_{0.71,0.27}$ for $\ell = 2$, $We_a = 0.71$ and $We_b = 0.27$ is represented as a function of the angular frequency Ω (grey curve). The black and red vertical lines denote the position of the two natural frequencies Ω_a and Ω_b, respectively, at which we measure $R_{0.71,0.27}$. Inverting system (3.8)–(3.9) gives an estimate of $\Lambda_{0.71}$ and $\Lambda_{0.27}$. Using these computed values of $\Lambda_{0.71}$ and $\Lambda_{0.27}$ we plot the theoretical expression of (3.7) at all frequencies (black line). This expression captures the main features of the ratio $R_{0.71,0.27}(\Omega)$: the low-frequency limit, the position and amplitude of the peak.

We then follow this procedure for every pair (We_a, We_b) and obtain 14 estimations of Λ_ℓ per Weber number per mode ℓ. We did not find a significant bias on the estimated value of $\Lambda_\ell(We)$ as a function of the Weber ratio We_a/We_b. We then average over all values of We_b values to estimate $\Lambda_\ell(We_a)$. The values of Λ_ℓ for $\ell = 2$ and $\ell = 3$ as a function of We, and their standard deviation, are reported in table 2. For $\ell \geq 4$, (3.5) fails to describe the ratio R_{ab}. Figure 4b shows Λ_ℓ as a function of We for $\ell = 2$ and $\ell = 3$ with error bars encoding the 95 % confidence interval. We find no clear variation of Λ_ℓ with We, especially for $\ell = 2$. When ℓ increases, the dissipation also increases, as smaller scales are more efficient at dissipating energy. The increase of Λ_ℓ with ℓ is compatible with the ℓ-dependency in a quiescent environment from Lamb (1932). From our observations we found the following expression for the damping factor:

$$\Lambda_\ell = 0.6(\ell + 2)(2\ell + 1), \tag{3.10}$$

which has been validated only for $\ell = 2$ and 3. In quiescent environments, the damping coefficient is also independent of We, $\Lambda_\ell^q = 8\sqrt{2}(\ell + 2)(2\ell + 1)Re(d)^{-1}$, as it originates from molecular diffusion in the liquid. However, we find $\Lambda_2 \approx 6.6\Lambda_2^q$. The surrounding flow field induces an additional effective damping. Experimentally, Ravelet *et al.* (2011) also observed an additional damping for bubbles rising in turbulence but attributed it to the presence of the wake. Yet, similar observations come from drop oscillations in space.
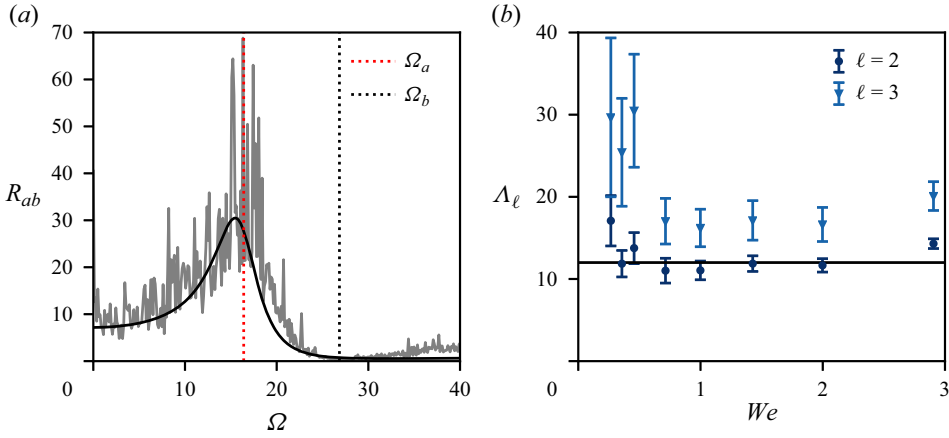
Figure 4. (a) Ratio between the Fourier spectrum at $We_a = 0.71$ and $We_b = 0.27$ for the mode $\ell = 2$. The red and black vertical lines denote the position of the Rayleigh frequency at these two We, where we evaluate R_{ab}. The black line results from (3.7). (b) Damping factor as a function of We for $\ell = 2$ and $\ell = 3$. The error bars encode the 95 % confidence interval $1.96\sigma_\Lambda/\sqrt{\#N}$, where σ_Λ is the standard deviation of Λ_ℓ and $\#N$ the number of samples. The solid black line corresponds to $\Lambda_2 = 12$.

We	2.9	2	1.43	1	0.71	0.46	0.36	0.27
Λ_2	14.3	11.7	11.9	11.0	11.0	13.8	11.9	17.1
σ_Λ^2	1.1	1.6	1.8	2.2	2.9	3.6	3.1	5.9
Λ_3	20.1	16.6	17.1	16.2	17.0	30.5	25.4	29.7
σ_Λ^3	3.3	4.0	4.6	4.4	5.3	13.1	12.5	18.5

Table 2. Average damping parameter Λ_ℓ and corresponding standard deviation, for every We.

In the presence of a turbulent internal flow, drop oscillations are significantly damped (Bojarevics & Pericleous 2003; Berry *et al.* 2005). This additional damping is interpreted in terms of a turbulent eddy viscosity (Xiao *et al.* 2021). In addition, Vela-Martín & Avila (2021) showed that there is a transfer of energy from the drop interface to eddies closer than $0.2\,d$ from the drop interface and inside the drop. They call them inner eddies. These small eddies efficiently dissipate energy. This transfer of energy suggests that the enhanced damping comes from an increase in the local effective diffusivity.

It is advantageous to estimate the size of an equivalent mixing length L_t. This characteristic length of momentum transport was first introduced by Prandtl (Boussinesq 1877; Prandtl 1949; Xiao *et al.* 2021) to describe, in a turbulent flow, the logarithmic profile of the velocity near a wall. By dimensional considerations, one can estimate the effective turbulent viscosity ν_t, using L_t and a typical velocity scale of velocity fluctuations at that scale, $\langle \delta u(L_t)^2 \rangle^{1/2}$,

$$\nu_t = \langle \delta u(L_t)^2 \rangle^{1/2} L_t = \sqrt{2}\epsilon^{1/3} L_t^{4/3}. \tag{3.11}$$

Expressing the effective damping rate in terms of this effective turbulent viscosity gives

$$\Lambda_\ell = 8(\ell+2)(2\ell+1)\frac{\nu_t d^{2/3}}{d^2\epsilon^{1/3}} = 8\sqrt{2}(\ell+2)(2\ell+1)\left[\frac{L_t}{d}\right]^{4/3}. \tag{3.12}$$

1001 A26-13

Injecting (3.10), gives an estimate for L_t

$$L_t = \frac{d}{10} = \frac{R_0}{5}. \tag{3.13}$$

Being of the same order of magnitude as the bubble radius, we hypothesize that the mixing length originates from a geometric effect, similar to the separation between inner and outer eddies from Vela-Martín & Avila (2021). We further investigate the origin of this effective damping in the last section, by looking at the local velocity gradients close to the bubble interface.

3.5. *Effective forcing statistics: temporal correlations and distribution*

Since the left-hand side of (3.1) is now completely determined, we can compute the right-hand side, and interpret it as a forcing term from the turbulent flow.

To interpret and comment on the statistics of the forcing term we will obtain, let us briefly discuss the physical origin of the forces acting on a bubble in a turbulent flow. To the best of our knowledge, there is no theoretical description of the forcing statistics acting on a bubble. For particles lying within the inertial range, the force exerted by the flow is often modelled by the Eulerian pressure gradient, integrated over the particle surface (Calzavarini *et al.* 2009), a framework that can also be applied to bubbles (Volk *et al.* 2008). Decomposed in the spherical harmonic base, the pressure on a sphere of radius R reads

$$p(\theta, \phi) = P_c \left[\sum_{\ell=0}^{\infty} \sum_{m=-\ell}^{\ell} P_{\ell,m}(t) \, Y_\ell^m(\theta, \phi) \right], \tag{3.14}$$

where $P_c = \rho \delta u(d)^2$ is a characteristic pressure fluctuation. There is no direct experimental measurement of these pressure coefficients. In practice, only two-point pressure measurements (pressure increments) have been studied. From force balance on a finite-size particle in a turbulent flow, the modes $\ell = 1$ are the components of the hydrodynamic force, equal to the Lagrangian particle acceleration. Practically speaking, the pressure increments are a good proxy for the Lagrangian particle acceleration.

For the higher-order modes ($\ell \geq 2$) there is no measurement in turbulence. Moreover, to describe deformations rather than motions, the framework used for particle acceleration cannot be simply extended. The interface deformations are primarily driven by the velocity gradients at the interface, which themselves depend on the presence of the bubble. Still, these gradients are closely related to the pressure statistics at the bubble scale. Therefore, from time to time, we will comment on our statistics of $\mathcal{T}_\ell$ ($\ell \geq 2$) in the light of P_1, namely the Lagrangian acceleration statistics and the pressure increment. A direct measure of the statistics of P_ℓ ($\ell \geq 2$) in the absence of bubble is provided in § 5.

Practically, we compute $\mathcal{T}_\ell$ from the modes' Fourier transform $\hat{x}_\ell$ using the following relation:

$$\mathcal{T}_\ell(t) = \frac{1}{2\pi} \int_{-\infty}^{\infty} \hat{x}_\ell(\Omega)(\Omega_\ell^2 - \Omega^2 + i\Lambda_\ell \Omega) e^{i\Omega t} d\Omega, \tag{3.15}$$

where we use the expressions of Λ_ℓ and Ω_ℓ from (3.4) and (3.10).

As expected from rotational invariance, we find that the average forcing $\langle \mathcal{T}_\ell \rangle$ vanishes for all *We*. The standard deviation of $\mathcal{T}_\ell$, $\sigma_{\mathcal{T}}^\ell$ is shown in figure 5 as a function of *We* for $\ell = 2$ and 3 (colour coded). Here, $\sigma_{\mathcal{T}}^\ell$ is found to be almost independent of the Weber number. We found that the effective forcing from the turbulent flow does not depend on
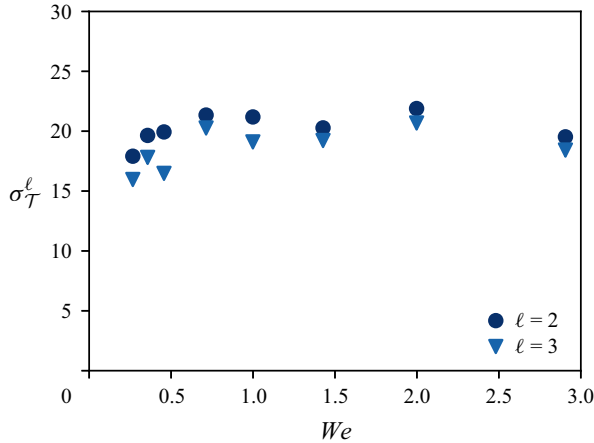
Figure 5. Standard deviation of $\mathcal{T}$ as a function of *We* for $\ell = 2$ and $\ell = 3$. No *We*-dependency is observed, while $\sigma_{\mathcal{T}}$ decreases slightly for larger ℓ.

bubble deformability. Therefore, bubble deformations are only one-way coupled to the flow.

In physical units, the force $\mathcal{T}_\ell$ then scales as $\alpha(\ell)\epsilon^{2/3}d^{-1/3}$, where α_ℓ is a function of the mode order. The standard deviation decreases with ℓ, compatible with $\alpha_\ell \sim \ell^{-1/2}$.

In the context of Lagrangian particle acceleration in turbulence, the standard deviation of acceleration also decreases with particle size as $d^{-1/3}$. This scaling can be predicted using a scale invariant pressure fluctuation argument (Voth *et al.* 2002; Qureshi *et al.* 2007; Volk *et al.* 2011). In addition, Lagrangian acceleration statistics do not depend explicitly on the Reynolds number at the particle size $Re(d)$, as long as the particle lies within the inertial range. Only a marginal effect of the flow Taylor Reynolds number Re_λ on the variance of the acceleration (Voth *et al.* 2002) was found. As a consequence, we expect the effective forcing to be independent of Re_λ, $Re(d)$ and the Weber number.

Beyond the first two moments of the effective forcing distribution, it is interesting to look at the full distribution. Figures 6(*a*) and 6(*b*) show the probability distribution of $\mathcal{T}_2$ and $\mathcal{T}_3$, respectively, for all *We*, normalized by their standard deviation $\sigma_{\mathcal{T}}^\ell$. We find that the shape of the distribution is also independent of the Weber number. These distributions are characterized by exponential tails, and are well described by the hyperbolic secant distribution (black dashed line)

$$\text{p.d.f.}(\mathcal{T}) = \frac{1}{2\sigma_{\mathcal{T}}^\ell}\operatorname{sech}\left(\frac{\pi}{2}\frac{\mathcal{T}}{\sigma_{\mathcal{T}}^\ell}\right), \tag{3.16}$$

which depends on a single parameter, the standard deviation $\sigma_{\mathcal{T}}^\ell$. The probability that a large forcing occurs is much larger than that of a Gaussian distribution (solid black line).

It is again tantalizing to compare this distribution with Lagrangian acceleration statistics for both particles and bubbles (Voth *et al.* 2002; Qureshi *et al.* 2007; Volk *et al.* 2008; Homann & Bec 2010; Prakash *et al.* 2012; Salibindla, Masuk & Ni 2021). For small, neutral tracers and particles of Kolmogorov-scale size, the acceleration distributions exhibit larger tails, decreasing slower than exponential. However, for larger particles ($d/\eta > 10$), the shape exhibits an exponential tail, independent of bubble size and therefore of $Re(d)$ (Voth *et al.* 2002; Qureshi *et al.* 2007; Volk *et al.* 2011). The p.d.f. shape of the Lagrangian acceleration is well described by the following expression, initially
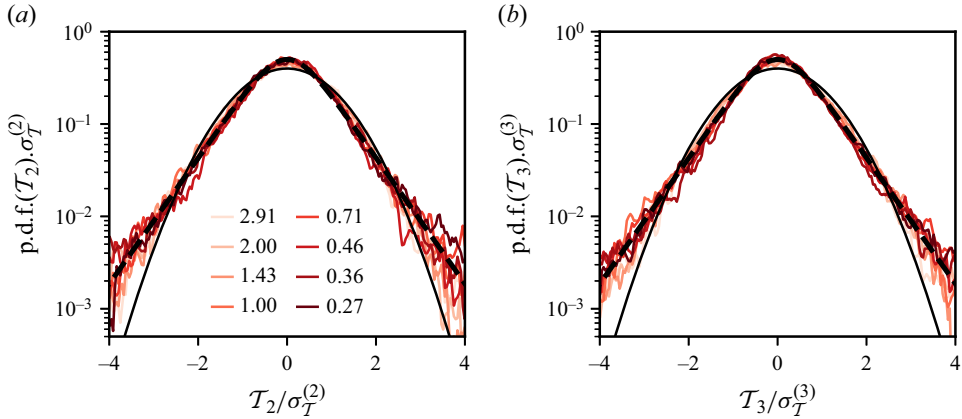
Figure 6. Probability density functions of $\mathcal{T}_2$ (*a*) and $\mathcal{T}_3$ (*b*) for all *We* (colour coded), normalized by their standard deviations. The shape of the distribution is independent of *We*. The dashed line represents the hyperbolic secant distribution, while the solid line is the Gaussian distribution.

proposed for tracer particles (Mordant, Crawford & Bodenschatz 2004; Qureshi *et al.* 2007):

$$\text{p.d.f.}(x) = \frac{e^{3s^2/2}}{4\sqrt{3}} \left[1 - \text{erf}\left(\frac{\log(|x/\sqrt{3}|) + 2s^2}{\sqrt{2}x} \right) \right], \tag{3.17}$$

where *x* is the standardized variable and *s* an additional fitting parameter. In the range of resolved scale, the two expressions, (3.16) and (3.17), are compatible with our experimental data.

To characterize the temporal evolution of the effective forcing $\mathcal{T}_\ell$, we study its ensemble-averaged Fourier transform $\langle|\hat{\mathcal{T}}_\ell|\rangle$. Injecting (3.4) and (3.10) within (3.5) we obtain an expression in Fourier space for $\langle|\hat{\mathcal{T}}_\ell|\rangle$

$$\langle|\hat{\mathcal{T}}_\ell|\rangle(\Omega) = \langle|\hat{x}_\ell|\rangle(\Omega) \cdot \left[(\Omega^2 - \Omega_\ell(We)^2)^2 + \Lambda_\ell^2 \Omega^2 \right]^{1/2}. \tag{3.18}$$

Figures 7(*a*) and 7(*b*) show $\langle|\hat{\mathcal{T}}_2|\rangle$ and $\langle|\hat{\mathcal{T}}_3|\rangle$, respectively, as a function of $\Omega\ell^{-2/3}$, where $\ell^{2/3}$ is the eddy turnover time at scale d/ℓ (in units of $t_c(d)$). For all frequencies, we found that the effective forcing spectrum does not depend on the Weber number. At low frequencies ($\Omega < 1.3\,\ell^{2/3}$), the forcing amplitude is constant, corresponding to a white noise. For $\Omega > 2\pi\ell^{2/3}$, the decay of $\langle|\hat{\mathcal{T}}_\ell|\rangle$ is compatible with $1/\Omega^2$. The limit between these two regimes is set by the eddy turnover time at scale d/ℓ. We found that the spectrum of the effective forcing only depends on the turbulence parameters, and is therefore independent of the bubble deformations. As was anticipated in § 3.1, model (3.1) decouples the turbulent forcing (the right-hand side) from the bubble response (the left-hand side). The observation of a cutoff frequency at the characteristic time scale of turbulent fluctuations at the mode scale d/ℓ can be interpreted as a filtering process originating from the integration over the bubble surface. This filtering operation is further discussed in § 5.

From the previous observations, we propose the following expression for the forcing spectrum:

$$\langle|\hat{\mathcal{T}}_\ell|\rangle(\Omega) = \frac{\tau_\ell}{1 + [\Omega\ell^{-2/3}/(2\pi)]^2}, \tag{3.19}$$
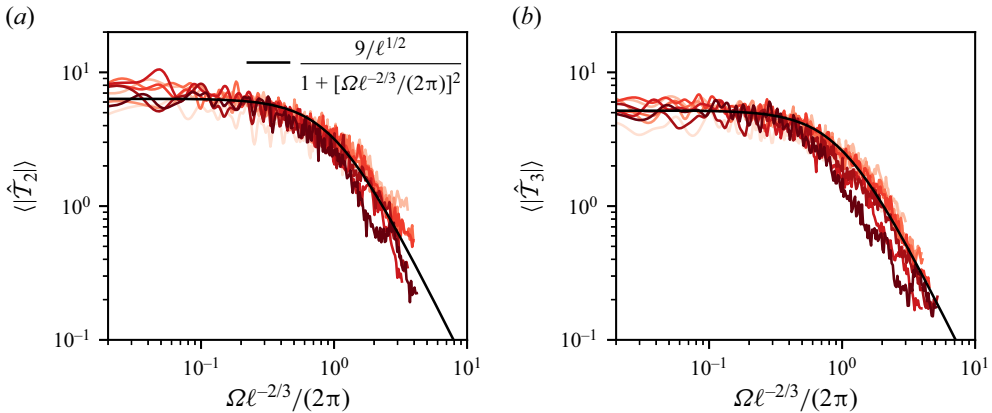
Figure 7. Effective forcing spectrum for $\ell = 2$ (*a*) and $\ell = 3$ (*b*) deduced from (3.18) as a function of the frequency normalized by the eddy turnover time at scale d/ℓ. The Weber number is colour coded with the same colour bar as in figure 2.

where τ_ℓ is a numerical constant, accounting for the ℓ-dependency of $\mathcal{T}_\ell$, that is adjusted on the data. From (3.6) and figure 3, we estimate $\tau_\ell \sim \ell^{-1/2}$. The expression (3.19) captures quantitatively the effective forcing spectrum (solid black line in figure 7(*a*,*b*).

In the context of Lagrangian particle accelerations, Voth *et al.* (2002), followed by Volk *et al.* (2008), computed the temporal autocorrelation of inertial particle accelerations in turbulence. The temporal acceleration statistics of a finite-size particle is usually attributed to a filtering effect of the small-scale turbulent fluctuations at the particle scale (Qureshi *et al.* 2007). As a consequence, the correlation time of acceleration for a neutrally buoyant particle is given by the eddy turnover time $t_c(d)$. This result has been recently extended to a buoyant particle that exhibits a modified correlation time $t \sim t_c(d)\beta^{-1/2}$ (Fan *et al.* 2024), where $\beta = 3\rho/(2\rho + \rho_p)$ is a function of the fluid density ρ and the particle density ρ_p. For a bubble, we have $\beta = 3$, corresponding to a correlation time of order t_c. In our case, the temporal auto-correlation function $C_{\mathcal{T}_\ell}(t) = \langle \mathcal{T}_\ell(0)\mathcal{T}_\ell(t)\rangle/(\sigma_{\mathcal{T}}^\ell)^2$ for the modes $\ell > 1$ can be deduced from the spectrum $\hat{\mathcal{T}}_\ell$ and is written as

$$C_{\mathcal{T}_\ell}(t) = \exp(-2\pi\ell^{2/3}t)(1 + 2\pi\ell^{2/3}t). \tag{3.20}$$

We found that the correlation time in physical units is given by $t_c(d)\ell^{-2/3}/(2\pi)$, which also scales as $t_c(d)$, with an additional dependency on the mode order ℓ. The prefactor being smaller than one, the mode oscillations decorrelate faster that the velocity fluctuations at the bubble scale.

In summary, we found that all the statistics of $\mathcal{T}_\ell$ are independent of *We*, which confirms the initial intuition of Risso & Fabre (1998) that the bubble dynamics and turbulent forcing are decoupled. We found that the bubble deformation by the flow field can be described by a one-way coupling model: the flow field generated by bubble oscillations does not significantly impinge back on the bubble dynamics. In addition, experimental results from the literature suggest that these statistics are likely to be independent of *Re*(*d*), as long as we consider bubbles larger than the Kolmogorov scale.

From the stationary hypothesis (H3), the forcing is completely characterized by its distribution and temporal autocorrelation function. The combination of an explicit form for the p.d.f. (3.16) and for the autocorrelation function (3.20) then provides a complete model of a synthetic stochastic effective forcing for bubble deformations in turbulence.
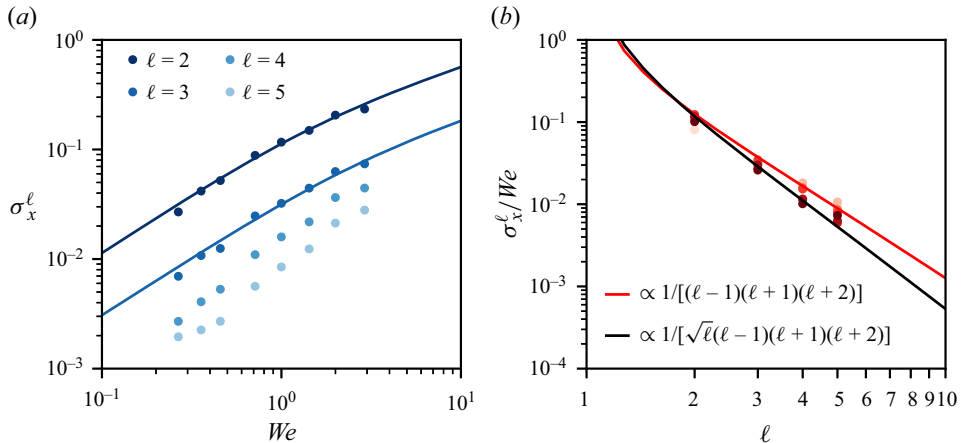
Figure 8. (*a*) Modes' standard deviation as a function of the Weber number for all ℓ. The two solid lines are the results from our linear model, for modes $\ell = 2$ and $\ell = 3$. (*b*) Modes' standard deviation compensated by *We* as a function of the mode principal number.

Previous modelling approaches have used two-point velocity measurements to model an effective forcing term (Risso & Fabre 1998; Lalanne *et al.* 2019; Masuk *et al.* 2021*b*), following the original idea from Kolmogorov (1949) and Hinze (1955). Here, we found that the statistics of the effective forcing differ significantly from two-point statistics, in particular due to the volumetric filtering effect at the particle size.

4. Model validation

To describe the bubble deformation, we have inferred step by step an equation including, damping, the natural frequency and a statistical model for the effective forcing term $\mathcal{T}_\ell$. To validate and draw the limits of our model, we compare the output of the linear model with our direct numerical simulation (DNS) data.

4.1. *Modes' standard deviation and distributions*

We first look at the modes' standard deviation σ_x^ℓ.

Figure 8(*a*) shows the modes' standard deviation of the DNS as a function of the Weber number for $\ell \in [2, 5]$. We find that σ_x^ℓ can be approximated by $\sigma_x^\ell \approx We/[(\ell - 1)(\ell + 1)(\ell + 2)]$, with a constant of order one. We compute σ_x^ℓ from the model in Fourier space using expressions of (3.4), (3.10) and (3.19) and the Parseval identity. The results are superimposed by the solid line for $\ell = 2$ and 3, showing a quantitative agreement with the numerical data.

A scaling for σ_x^ℓ as a function of *We* and ℓ can be deduced analytically in model cases. One natural case is to consider $\mathcal{T}_\ell$ as a Gaussian white noise of autocorrelation function $C(t) = D\delta(t)$, where δ is the Dirac function, and D is independent of the Weber number. In this case, from the analysis of stochastic harmonic oscillators (Gitterman 2005), the standard deviation reads

$$\sigma_x^\ell \sim \left[\frac{D}{\Lambda_\ell \Omega_\ell^2} \right]^{1/2}. \tag{4.1}$$

From the coefficients Λ_ℓ and Ω_ℓ we extracted, this model predicts $\sigma_x^\ell \propto We^{1/2}$, which does not correspond to the observed scaling. A finite correlation time has been taken into account. We then consider $\mathcal{T}_\ell$ as an exponentially correlated Gaussian noise of autocorrelation function $\langle \mathcal{T}_\ell(t)\mathcal{T}_\ell(t') \rangle = (\sigma_\mathcal{T}^\ell)^2 \exp(-|t-t'|/t_\ell)$, where $t_\ell = \ell^{-2/3}/(2\pi)$ is the correlation time of the effective forcing deduced from (3.20), and D is independent of We. In this case, the mode's standard deviation reads (Gitterman 2005)

$$\sigma_x^\ell = \sigma_\mathcal{T}^\ell \left[\frac{t_\ell(1+\Lambda_\ell t_\ell)}{\Omega_\ell^2 \Lambda_\ell(1+\Lambda_\ell t_\ell + \Omega_\ell^2 t_\ell^2)} \right]^{1/2}. \tag{4.2}$$

The scaling of σ_x^ℓ now becomes a function of the ratios $\Lambda_\ell t_\ell$ and $\Omega_\ell t_\ell$. In practice, we have $\Omega_\ell t_\ell \gg 1$ and $\Omega_\ell t_\ell \gg \Lambda_\ell t_\ell$ for sufficiently small Weber. Considering the limit $\Lambda_\ell t_\ell \gg 1$, (4.2) simplifies as

$$\sigma_x^\ell = \frac{\sigma_\mathcal{T}^\ell}{\Omega_\ell^2} = \frac{\sigma_\mathcal{T}^\ell}{(\ell-1)(\ell+1)(\ell+2)} We. \tag{4.3}$$

We then recover the observed scaling for small Weber number. For larger Weber number, the ratio $\Omega_\ell t_\ell$ decreases, and we expect a transition to a shallower increase of σ_x^ℓ with We. This transition should occur for larger Weber number as ℓ increases, an interpretation compatible with the numerical data shown in figure 8(*a*). The observed scaling of σ_x^ℓ with Weber number thus corresponds to a saturation of the bubble deformations dominated rather by the long correlation time of the forcing (frozen turbulence hypothesis applied to bubble deformations Ruth *et al.* 2019) than an accumulation of random forcing events on a time scale $1/\Lambda_\ell$. It is worth noticing that the estimate of the correlation time of the forcing is therefore essential to predict the amplitude of bubble deformations.

To further check the dependency on ℓ, figure 8(*b*) shows the compensated standard deviation σ_x^ℓ/We. We recover that the decrease of the modes' amplitude with ℓ can be mainly attributed to the increase of the natural frequency with ℓ, with a small correction originating from the weak dependency of $\mathcal{T}_\ell$ with ℓ. Eventually, we found a quantitative agreement between the standard deviation x_ℓ and the result from the linear model. The model captures the evolution of σ_x^ℓ with both We and ℓ.

The linear increase of σ_x^ℓ with We, up to $We \approx 3$, has important consequences when modelling bubble breakup. Risso & Fabre (1998) suggested that the threshold for breakup is close to the value above which the deformations start to be nonlinear. A linear model would then be sufficient to describe bubble deformations up to the breakup threshold.

We then look at the entire statistics of x_ℓ. Figure 9 shows the probability density functions of the modes $\ell = 2$ for all Weber numbers (9*a*) normalized by their standard deviation. We find that the shape of the p.d.f. does not depend on the Weber number and corresponds to the hyperbolic secant distribution (black dashed line), equivalent to the p.d.f. of the effective force $\mathcal{T}_\ell$. Both the forcing and the mode amplitude share the same p.d.f. that deviates from Gaussianity (solid black line) with exponential tails. As the distributions exhibit fat tails, the probability that bubbles experience large deformations leading to breakup is large compared with a Gaussian distribution (black dotted line). Moreover, for larger ℓ, the deviation from a Gaussian distribution increases, as shown in figure 9(*b*) for $We = 1$.
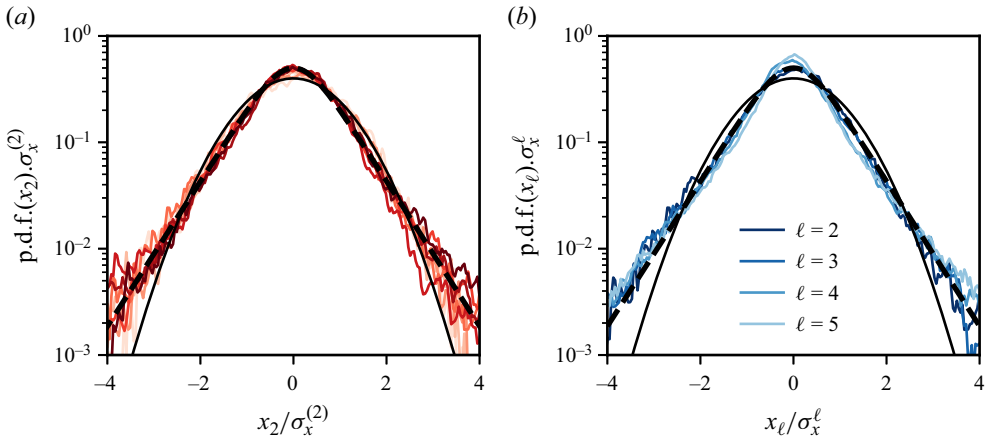
Figure 9. (*a*) Normalized p.d.f. of x_2 for all *We*. (*b*) Normalized p.d.f. at $We = 1$ for different ℓ. In both panels the black dashed line is the hyperbolic secant distribution. The solid black line the Gaussian distribution.
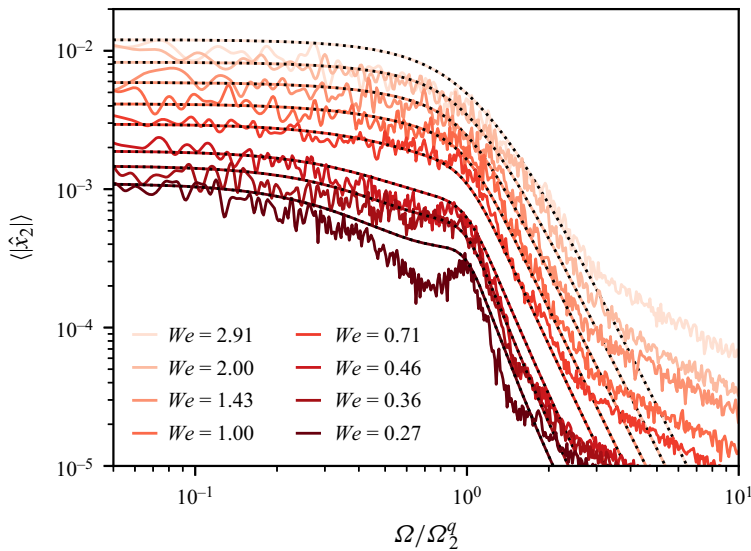

Figure 10. Comparison of the Fourier spectrum amplitude between the DNS and the model (dotted line). The model spectrum is obtained by combining (3.10), (3.4) and (3.19) in (3.5), for the mode $\ell = 2$. The model captures the low-frequency limit, the position of the transition as well as the high-frequency decay for all *We*.

4.2. *Deformation spectrum*

Figure 10 compares the modes' Fourier transforms with the model (3.5) combined with (3.10), (3.4) and (3.19) (dotted lines). For all Weber numbers, the model accurately reproduces the zero-limit frequency as well as the amplitude of the spectrum at the bubble natural frequency f_2 and the position and slope of the decay at larger frequencies. At the lowest Weber number ($We = 0.27$), the model overestimates the spectrum just below the resonance. We remind the reader here that, for angular frequencies larger than $3\Omega_2$, the spectrum is dominated by numerical noise. For all other *We*, in the absence of resonance, the model captures the spectrum close to the bubble natural frequency.

4.3. *Consequences for bubble breakup*

Thanks to the quantitative model we have developed, we can revisit the breakup scenario and the criterion for breakup. Two main breakup scenarios have been proposed for bubbles in turbulence. Bubbles can break either when they encounter a turbulent fluctuation larger than some threshold value (Lee *et al.* 1987; Luo & Svendsen 1996; Wang *et al.* 2003; Masuk *et al.* 2021*a*) or after a series of small excitations at their natural frequency which induce a resonance (Sevik & Park 1973; Risso & Fabre 1998). The ability of a bubble to store energy in a mode ℓ, is quantified by the quality factor $Q_\ell = \Omega_\ell / \Lambda_\ell$. The quality factor Q_ℓ sets the number of periods over which energy can be stored. For large Q_ℓ, energy can be accumulated, while it is dissipated in a few bubble periods for low Q_ℓ. Our linear model provides a quantitative measure of Q_ℓ. Combining (3.4) and (3.10) we have an explicit expression for Q_ℓ as a function of *We* and ℓ

$$Q_\ell = 4\sqrt{\frac{(\ell - 1)(\ell + 1)}{0.6(\ell + 2)(2\ell + 1)^2}} We^{-1/2}. \tag{4.4}$$

In turbulence, bubbles mainly break after oblate–prolate deformations, meaning deformations along their second modes $\ell = 2$ (Risso & Fabre 1998; Ravelet *et al.* 2011; Masuk *et al.* 2021*b*; Perrard *et al.* 2021). For the typical critical Weber numbers reported in the literature, $0.1 < We_c < 10$ (Sevik & Park 1973; Risso & Fabre 1998; Martínez-Bazán, Montanes & Lasheras 1999; Rivière *et al.* 2021), our estimate of the quality factor for the mode $\ell = 2$ ranges from 0.3 ($We_c = 10$) to 3 ($We_c = 0.1$). These quality factors are too small to observe significant energy storage over several periods of oscillations. Resonance can still occur for the largest $Q_\ell \approx 3$. However, we expect the resonant mechanism to be subdominant at this quality factor. We conclude that bubbles break from short and large turbulent fluctuations rather from a series of small excitations at the bubble natural frequency (resonant mechanism).

Note that a sequence of oscillations at the bubble natural frequency may be observed for sufficiently large quality factor, typically $Q_2 > 10$, corresponding to $We < 8 \times 10^{-3}$. Even though such a Weber number corresponds to a bubble size much smaller than the Kolmogorov Hinze scale, which will never break, a resonant breakup may be observed experimentally.

5. Link between model coefficients and surrounding turbulent fields

In this section, we aim at connecting the effective variables we identified, namely the forcing $\mathcal{T}_\ell$ and the damping coefficient Λ_ℓ, to flow statistics in turbulence. The presence of a bubble modifies the flow statistics in its surrounding, through dynamical boundary conditions at the interface and incompressibility. Nevertheless, for drops, it has been shown that the outer eddies (further than $0.2d$ from the interface) generate most of the normal stress (Vela-Martín & Avila 2021). These outer eddies may be less affected by the presence of the interface. Therefore, it is natural to compare the flow statistics on a sphere in the absence of a bubble with the effective force statistics. In § 3.5, we argued that the pressure modes are a good proxy for the effective forcing. In this section, we then compare the statistics of $\mathcal{T}_\ell$ with the pressure modes' statistics in the single-phase case. On the other hand, the damping is expected to give rise to eddies contained in the boundary layer near the interface (Vela-Martín & Avila 2021). To rationalize the origin of the additional damping from the flow statistics, we will therefore study the local dissipation in the bubble boundary layer.
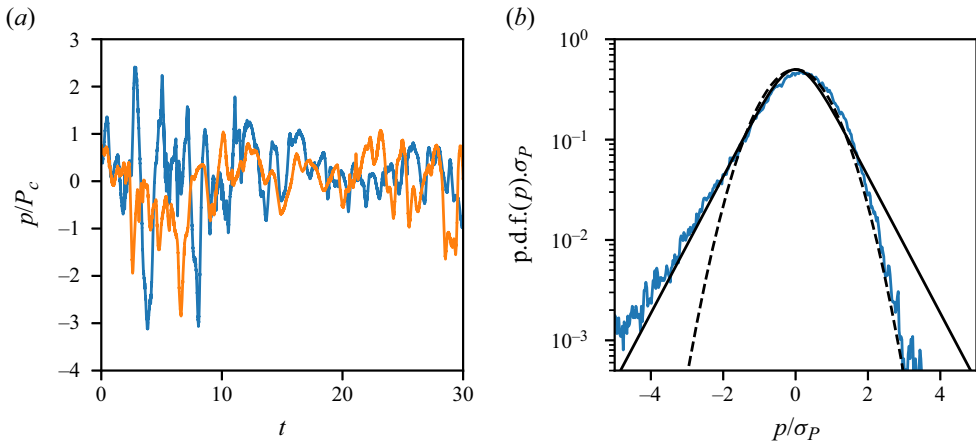
Figure 11. (*a*) Typical temporal evolution of the pressure at two points in space. We observe small-amplitude oscillations together with rare intense negative peaks. (*b*) Local pressure distribution normalized by its standard deviation $\sigma_p = 0.67P_c$. The solid black line follows the hyperbolic secant distribution centred while the black dashed line follows a Gaussian distribution with standard deviation 4/5.

5.1. *Point statistics of the pressure field*

As a reference case, we first consider the Eulerian point statistics of pressure in homogeneous and isotropic turbulence, at the same Taylor Reynolds number $Re_\lambda = 55$, corresponding to the two-phase flow case. To compare with the bubble dynamics, we will still express length scales in units of d, time scales in units of $t_c(d)$ and therefore velocity in terms of velocity increments at the bubble scale $\langle\delta u(d)^2\rangle^{1/2}$.

We run single-phase DNSs and record the Eulerian pressure fluctuations $p(x, t)$ at seven different fixed locations well separated in space. We run three simulations for a total of $245t_c(d)$. Resolution is increased compared with the two-phase problem and would be equivalent to 68 points per bubble radius and 3.6 points per Kolmogorov length. Note that increasing the resolution was not necessary but allows us to obtain more precise results, especially in the viscous range. In this section, ensemble averages are performed over the three simulations and the seven locations.

Figure 11(*a*) illustrates two temporal evolutions of pressure, normalized by the characteristic pressure difference at the bubble scale, $P_c = \rho\delta u(d)^2$. We found a pressure standard deviation $\sigma_p = 0.67P_c$. Pressure exhibits random oscillations of small amplitude around zero, together with large negative drops. This asymmetry between positive and negative fluctuations is better observed on the pressure p.d.f. plotted in figure 11(*b*). We recover that negative values are exponentially distributed, while positive values follow a Gaussian distribution (dashed black line). The existence of the large negative peaks leading to an asymmetric p.d.f. is well known and has been reported both in experiments (Abry *et al.* 1994; Pumir 1994; Cadot, Douady & Couder 1995) and DNSs of homogeneous isotropic turbulence (Cao, Chen & Doolen 1999; Vedula & Yeung 1999). It has been shown that these large negative peaks correspond to vorticity filaments (Douady, Couder & Brachet 1991; Fauve, Laroche & Castaing 1993; Cadot *et al.* 1995) passing through the measurement point. As the bubble moves in the fluid, it may experience different pressure statistics and the Lagrangian pressure statistics could also be relevant.

Lagrangian pressure statistics have also been investigated numerically. Numerical studies involve measuring pressure statistics along the paths of point particles (Bappy,
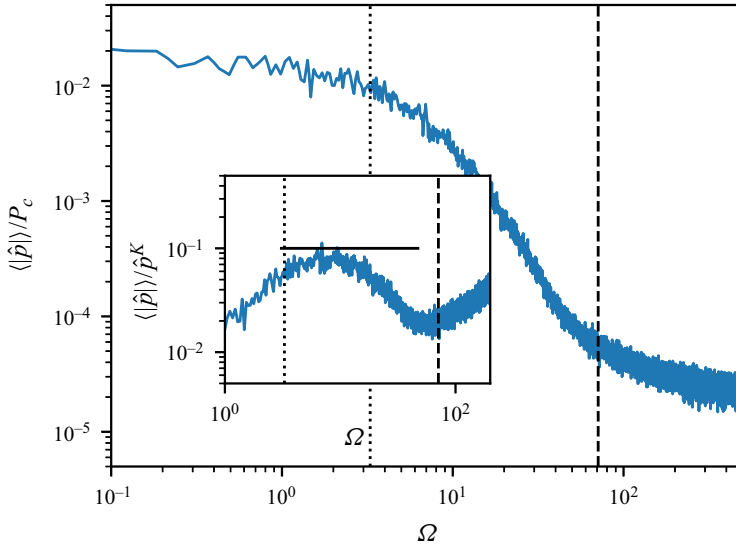
Figure 12. (*a*) Amplitude of the local pressure Fourier transform. The vertical dotted line corresponds to the angular frequency $\Omega_c(L)$ of eddies of integral length scale in size, while the dashed line corresponds to the angular frequency $\Omega_c(\eta)$ of eddies of Kolmogorov length scale in size. Inset plot: compensated Fourier transform $\langle|\hat{p}|\rangle/\hat{p}^K$. The solid line corresponds to $\langle|\hat{p}|\rangle = \hat{p}^K/10$.

Carrica & Buscaglia 2019), as well as (sub-Kolmogorov) finite-size bubbles (Bappy *et al.* 2020*a*,*b*) whose dynamics is modelled using a pure advection or a Maxey–Riley equation (Maxey & Riley 1983; Toschi & Bodenschatz 2009), respectively. They found that larger particles have a higher probability of being within low pressure regions. Nevertheless, the overall shape of the pressure p.d.f., with an exponential tail for negative values and a Gaussian distribution of positive values, is conserved.

To investigate the frequency statistics of the local pressure, we compute the temporal Fourier transform of each pressure signal $\hat{p}$

$$\hat{p}(\Omega) = \frac{1}{T}\int_0^T p(t)\mathrm{e}^{-\mathrm{i}\Omega t}\,\mathrm{d}t. \tag{5.1}$$

The average amplitude of its Fourier transform $\langle|\hat{p}|\rangle$ is plotted in figure 12. The corresponding inertial range in frequency space is delimited by the inverse of the eddy turnover time at the integral scale $\Omega_c(L) = 2\pi/t_c(L)$ (black dotted line) and the inverse of the eddy turnover time at the Kolmogorov scale, $\Omega_c(\eta)$ (dashed line). For low frequencies, $\Omega < \Omega_c(L)$, $\langle|\hat{p}|\rangle$ slowly decreases with Ω. Abry *et al.* (1994) have shown that this evolution at low frequencies originates from the contribution of vorticity filaments, since their typical lifetime is the integral time scale (Douady *et al.* 1991; Pumir 1994). Removing their contributions flattens the low-frequency spectrum (Abry *et al.* 1994).

In the inertial range of the turbulent cascade, $\Omega_c(L) < \Omega < \Omega_c(\eta)$, $\langle|\hat{p}|\rangle$ decays down to the noise level near $\Omega_c(\eta)$. In the spatial Fourier space, and *a fortiori* in the temporal Fourier space, there is no consensus for the scaling of the pressure power spectrum within the inertial range (Pullin & Rogallo 1994). A Kolmogorov-like scaling predicts $|\hat{p}(k)|^2 \sim \epsilon^{4/3}k^{-7/3}$ with k the mode's wave number (reported by Ishihara *et al.* (2003) for instance) but other authors have also reported a $k^{-5/3}$ scaling (Gotoh & Rogallo 1999; Vedula & Yeung 1999). To transform the spatial power spectrum into a temporal power
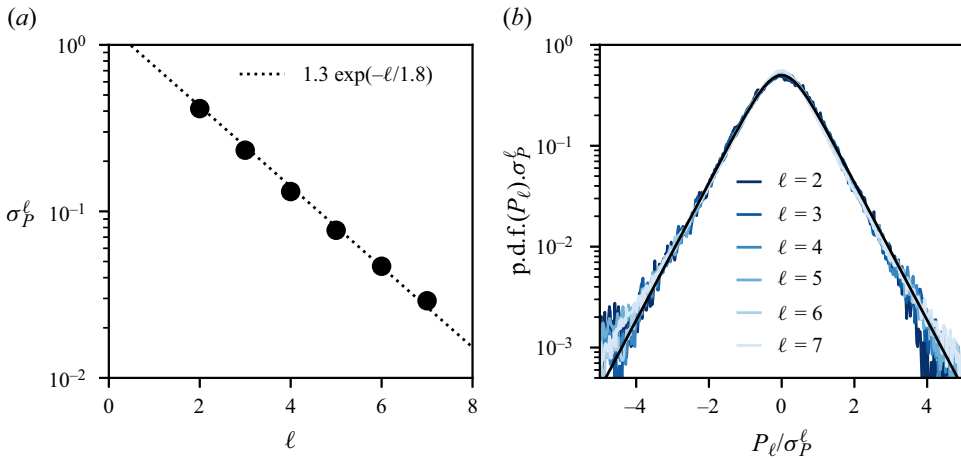
Figure 13. (*a*) Pressure standard deviation, σ_P^ℓ as a function of ℓ, showing an exponential decay with ℓ (black dotted line). (*b*) Distributions of P_ℓ, normalized by σ_P^ℓ, as a function of ℓ. All the pressure modes share the forcing distribution given in (3.16).

spectrum, a classical way is to consider that the small-scale structures are advected by the large scales. This is the sweeping hypothesis (Kraichnan 1964; Tennekes 1975), which has been successfully used to reproduce pressure temporal autocorrelation (Yao *et al.* 2008). Combining this argument with the Kolmogorov prediction, we find that $\langle \hat{p} \rangle$ should scale as $\hat{p}^K \sim \epsilon^{2/3} u_{rms}^{5/6} \Omega^{-4/3}$, with a proportionality constant of order 1. We find a reasonable agreement, as shown by the compensated spectrum $\langle \hat{p} \rangle / \hat{p}^K$ in the inset of figure 12. As evidenced by Pumir (1994), Pullin & Rogallo (1994) and Vedula & Yeung (1999), the Kolmogorov scaling might only hold in a narrow range of frequencies, corresponding to scales just below the integral scale, due to the limited inertial range. The proportionality constant is around 0.1 in our case (solid black line) lower than the value of 7 proposed by Pumir (1994). The third regime $\Omega > \Omega_c(\eta)$, corresponds to the end of the inertial range and is close to the limit of resolution of our DNS, as $\Omega_c(\Delta x) = 3\Omega_c(\eta)$, where Δx is the minimum grid size.

5.2. *Pressure field on a sphere*

To compare the pressure statistics with the effective forcing $\mathcal{T}_\ell$, we interpolate the pressure field $p_S(\theta, \phi)$ in the single-phase DNS on a sphere of radius R_0, and compute its spherical harmonic decomposition

$$p_S(\theta, \phi) = P_c \left[\sum_{\ell=0}^{\infty} \sum_{m=-\ell}^{\ell} P_{\ell,m}(t)\, Y_\ell^m(\theta, \phi) \right]. \tag{5.2}$$

Similarly to the modes of deformation $x_{\ell,m}$, the statistics of $P_{\ell,m}$ are independent of m. Ensemble averages are then computed over the three simulations and the m values. For pressure, the modes $\ell = 0$ and $\ell = 1$ are non-zero, however, we focus in the following on modes $\ell \geq 2$, which are relevant for bubble deformations. Figure 13(*a*) shows that the standard deviation of each mode ℓ, σ_P^ℓ, varies exponentially with ℓ. A higher ℓ is associated with fluctuations at a smaller scale, which are known to be less energetic. However, we have no explanation for the exponential scaling. We also observed a decay
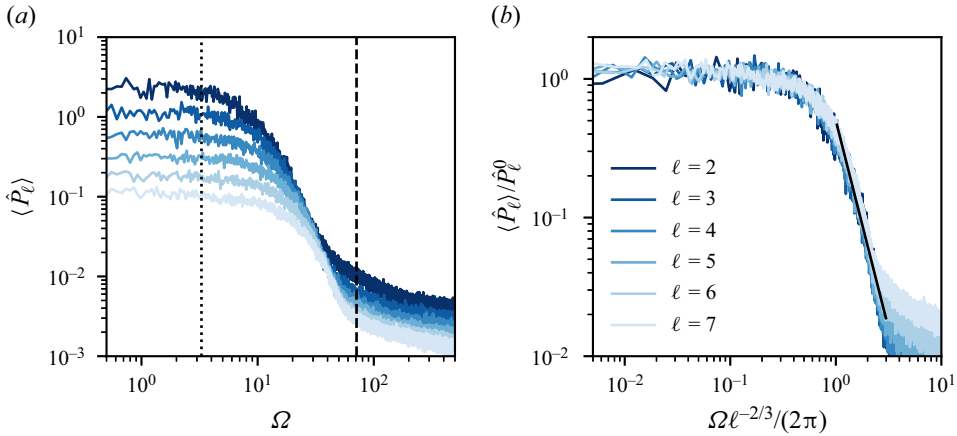
Figure 14. (*a*) Amplitude of the pressure Fourier transform $\langle|\hat{P}_\ell|\rangle$ for each mode ℓ as a function of the angular frequency in units of the eddy turnover time at the bubble scale. The black dashed line represents the eddy turnover time at scale η. The black dotted line is the eddy turnover time at the integral length scale. (*b*) Normalized pressure Fourier transform as a function of frequency in units of the eddy turnover time at scale d/ℓ. The black line follows Ω^{-3}.

of $\sigma_{\mathcal{T}}^\ell$ with ℓ (figure 5). The symmetry between positive and negative values is restored, as shown in figure 13(*b*). Distributions now show exponential tails for both negative and positive pressure values. The shape of the distribution is found to be independent of ℓ, corresponding to the same hyperbolic secant distribution (3.16) as the effective forcing distribution we previously identified.

Eventually, we compute the temporal Fourier transform $\hat{P}_\ell$ of the spherical pressure modes P_ℓ. Figure 14(*a*) shows the ensemble average of the norm, $\langle|\hat{P}_\ell|\rangle$ as a function of the frequency. For each ℓ, we recover the three regimes we observed for the point pressure spectrum and $\mathcal{T}_\ell$. The transition between the two first regimes depends on the mode ℓ. Considering that the pressure spectrum shares the same characteristic frequency as the effective forcing spectrum, we expect the transition to occur at $\Omega = 2\pi\ell^{2/3}$, the frequency associated with eddies of size d/ℓ, in units of $t_c(d)$. We show in figure 14(*b*) the spectra $\langle|\hat{P}_\ell|\rangle$ normalized by their low-frequency limit, $\hat{P}_\ell^0$, as a function of the frequency normalized by $\ell^{2/3}$, the eddy turnover time at scale d/ℓ. All curves collapse onto a single master curve, showing that the pressure and effective forcing share the same time scales. Below the critical frequency ($\Omega < \Omega_\ell$), the spectrum amplitude converges to a constant value, significantly above the integral frequency Ω_L. Similarly to Abry *et al.* (1994), the pressure spectrum at low frequency is now constant. We can assume that the averaging over the sphere has filtered the contribution from localized structures, and in particular the vorticity filaments. A flat spectrum in the range $\Omega_c(L) < \Omega < 2\pi\ell^{2/3}$ also indicates that the contribution of eddies larger than d/ℓ, which are roughly homogeneous at the mode scale, has also been filtered out: a bubble is mainly deformed by eddies at its scale. For $2\pi\ell^{2/3} < \Omega < \Omega_\eta$, $\langle|\hat{P}_\ell|\rangle$ follows Ω^{-3}. This decay is steeper than the ℓ-dependency of $\langle|\hat{\mathcal{T}}_\ell|\rangle$ which follows Ω^{-2}. This might be attributed to the discrepancy between Eulerian and Lagrangian statistics. From the sweeping effect (Kraichnan 1964), the temporal decorrelation of Eulerian quantities is expected to occur faster than their Lagrangian counterpart.

To summarize, we have shown that the effective forcing $\mathcal{T}_\ell$ deforming a bubble shares the same statistics as the corresponding pressure mode on a sphere of the same radius.

As a consequence of the filtering effect induced by the integration over a sphere, the characteristic frequency associated with each mode ℓ is the eddy turnover time at scale d/ℓ, the frequencies smaller than $\ell^{2/3}$ are well described by a white noise and the forcing amplitude decreases with ℓ.

5.3. *Dissipation profiles*

Our analysis of bubble deformation shows that (i) the effective forcing originates from turbulent fluctuations near the bubble, and it is not affected by bubble deformability. (ii) The damping of bubble oscillations is significantly enhanced compared with the quiescent case. This damping can either originate from additional dissipation in the turbulent boundary layer or an energy transfer from the bubble oscillations to the turbulent flow. Both mechanisms depend on the boundary layer thickness. Using a turbulent viscosity hypothesis we estimated that energy was transported on a boundary layer of size $L_t = R_0/5$, independent of *We*. In this section we investigate the velocity gradient profile near the bubble, on a distance comparable to bubble typical deformation. To do so, we need to compute a local distance r to the interface, which is not provided by the Basilisk volume of fluid (VOF) algorithm.

The method principle is the following. For every bulk point, we find the closest grid point on the interface. We then interpolate the bubble surface around this point, using a quadratic interpolation on the 20 closest neighbouring interfacial points. To find the neighbours efficiently, the interfacial grid points are stored in a $k - d$ tree structure. The distance r to the interface is then found by minimizing the distance from the bulk point to the quadratic manifold. We follow this procedure for both outside ($r > 0$) and inside ($r < 0$) bulk points.

We diagnose the additional dissipative term of the linear model by investigating the local dissipation rate profile around the bubble. The energy dissipation rate per unit of mass in a elementary volume is related to the local velocity gradients by

$$\langle \epsilon \rangle (x) = 2\nu \langle (\partial_i u_j + \partial_j u_i)^2 \rangle, \tag{5.3}$$

where we use Einstein notations. For each run, we output snapshots of the full flow field at times separated by at least one eddy turnover time at the bubble scale, to ensure statistical independence. We then compute profiles of the local dissipation near the interface by averaging on shells of constant distance from the bubble interface, as illustrated in figure 15. Eventually, for each Weber number, we ensemble average the flow snapshots (see table 3) to extract a mean profile.

Figure 16(*a*) shows the average local dissipation, divided by the kinematic viscosity, $\langle \epsilon \rangle (r)/\nu$, as a function of the distance r to the bubble interface. Far from the bubble interface, for $r > R_0/2$ and $r < -R_0/2$, the local dissipation converges to a constant. In the gas, velocity gradients are maximum at $r = -R_0/15$. The existence of a maximum inside the bubble near the interface originates from the nearly no-slip boundary condition imposed by the denser fluid on the gas inside the bubble. A similar boundary layer has indeed been observed near a solid particle's surface (no-slip boundary condition) (Shen *et al.* 2022; Chiarini & Rosti 2024). For bubbles, we therefore expect that decreasing the gas density increases the amplitude of the peak. The velocity gradients inside and outside the bubble share the same order of magnitude: the dissipation hence mainly takes place outside the bubble, in the liquid, where the dynamical viscosity is much larger. To understand the origin of the additional damping we then focus on the outside boundary layer.
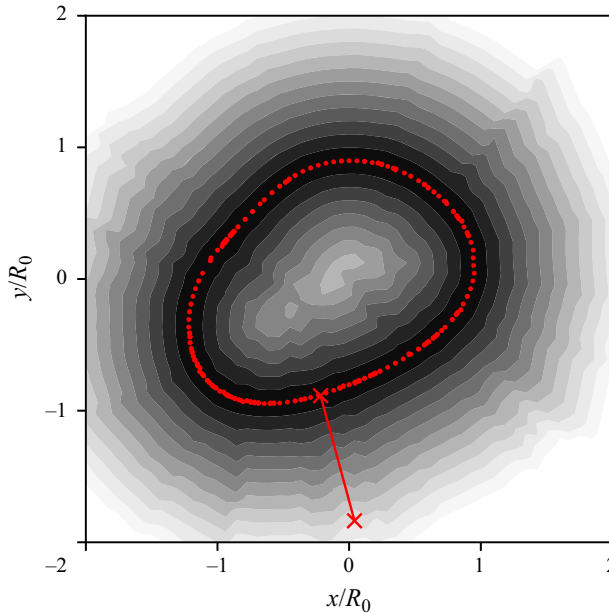
Figure 15. Example of the distance computation on a slice of a bubble at $We = 2$. The red points are on the interface. Isocontours are separated by $0.0625R_0$. We also show the association between one bulk points and the corresponding interfacial point.

We	2	1.43	1	0.71	0.46	0.36	0.27
N	48	68	68	27	46	24	52

Table 3. Number of snapshots per Weber number used to compute the flow profiles.

For $r > 0$, we observe a thick boundary layer of typical size $R_0/5$ (see figure 16a), compatible with our estimation of L_t (see (3.13)). Figure 16(b) shows the dissipation rate value at the interface in the liquid $\langle \epsilon \rangle|_{0^+}$ as a function of the Weber number. At vanishing Weber number, we find a non-zero dissipation originating from a geometrical boundary layer. The interfacial value varies between 3 times ($We = 0.27$) and four times ($We = 2$) larger than that in the bulk. In addition, we find an increase compatible with a linear dependency of the interfacial dissipation with We. If we interpret this additional dissipation as an energy transfer rate from the surface deformation to the flow, it would scale as $\Lambda_\ell (\dot{x}_\ell)^2$. We have $(\dot{x}_\ell)^2 \sim (\omega_\ell^q \sigma_x^\ell)^2 \propto We$. This interpretation is therefore compatible with a damping coefficient Λ independent of We.

In the absence of flow, the thickness of the boundary layer of the oscillating bubble can be estimated by $\sqrt{2\nu/\omega_2^q}$. For a Weber number ranging from 2.9 to 0.27, this estimation gives a boundary layer of size ranging from $0.07R_0$ to $0.04R_0$, which is much thinner than the boundary layer thickness we measured. We conclude that the boundary layer is geometric. It is not produced by bubble oscillations. The existence of a thick boundary layer was completely disregarded in the computation of Lamb (1932) for a potential flow far from the interface. The thick boundary layer we observed for the dissipation profile
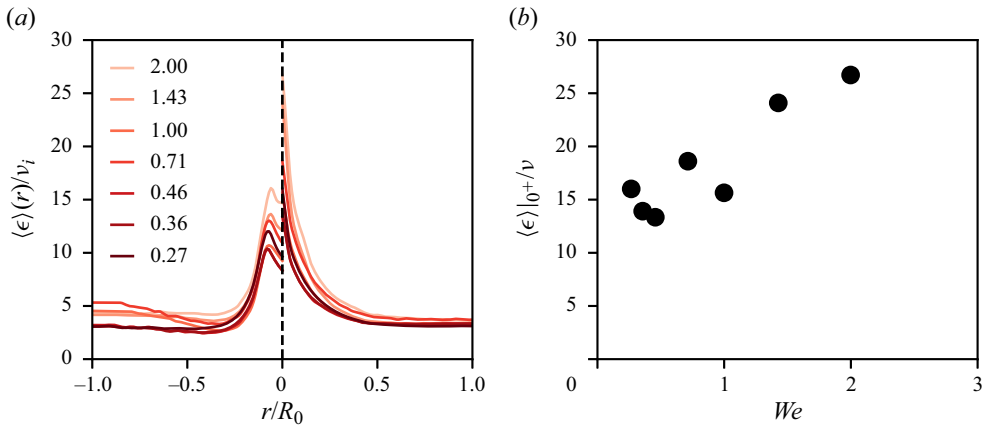
Figure 16. (*a*) Local velocity gradient inside and outside the bubble as a function of the distance to the interface, for all *We*. (*b*) Limit of the dissipation rate at the bubble interface in the liquid phase as a function of the Weber number.

is then consistent with an effective damping one order of magnitude larger than in the quiescent case.

6. Conclusion

In summary, we have shown that the deformations of bubbles in turbulence can be described in terms of a stochastic linear oscillator on the Rayleigh modes of oscillations up to a Weber of order unity. Conversely to previous works, we have directly measured, using DNS of bubbles in turbulence, the coefficients of this reduced model, namely, the damping rate and the natural frequency, together with the statistical properties of the effective forcing. We have shown that the natural frequency associated with each mode of deformation is not modified compared with the quiescent case. For the effective damping coefficient, we found that the damping is one order of magnitude larger than the prediction from Lamb. Looking at the dissipation profiles near the interface, we confirmed that the additional damping originates from a thick geometrical boundary layer of size $L_t \approx R_0/5$ in our case. In physical units, we expect the damping coefficients Λ_ℓ to scale as $\nu/d^2 Re(d)$. Eventually, we found that the effective forcing does not depend on the Weber number. This observation confirms that bubble deformations are one-way coupled to the flow: the back reaction of bubble deformations on the surrounding turbulent flow can be neglected. This effective forcing is characterized by a probability distribution with exponential tails and a typical correlation time which scales with the eddy turnover time at the mode's scale $t_c(d/\ell)$. We also looked at the statistics of pressure fluctuations on a sphere in the absence of bubbles, and we showed that the effective forcing shares the same p.d.f. as the pressure modes' p.d.f. as well as the same characteristic time scale. Due to the enhanced damping compared with the quiescent case, we showed that the resonant oscillation mechanism is not statistically relevant to explaining breakups. Indeed, at a Weber number of order unity, the bubble cannot accumulate deformation energy on several periods of oscillations as the quality factor $Q_2 = \Omega_2/\Lambda_2$ of the main bubble oscillations is too small. As a consequence, bubbles break rather from short and large turbulent fluctuations than from a series of small-amplitude excitations at the bubble natural frequency (resonant mechanism).

Declaration of interests. The authors report no conflict of interest.

Author ORCIDs.

Aliénor Rivière https://orcid.org/0000-0002-5658-0759;

Stéphane Perrard https://orcid.org/0000-0002-9315-2892.

REFERENCES

ABRY, P., FAUVE, S., FLANDRIN, P. & LAROCHE, C. 1994 Analysis of pressure fluctuations in swirling turbulent flows. *J. Phys.* **4** (5), 725–733.

ABU-AL-SAUD, M.O., POPINET, S. & TCHELEPI, H.A. 2018 A conservative and well-balanced surface tension model. *J. Comput. Phys.* **371**, 896–913.

BAPPY, M., CARRICA, P.M. & BUSCAGLIA, G.C. 2019 Lagrangian statistics of pressure fluctuation events in homogeneous isotropic turbulence. *Phys. Fluids* **31** (8), 085111.

BAPPY, M.H., CARRICA, P.M., VELA-MARTÍN, A., FREIRE, L.S. & BUSCAGLIA, G.C. 2020*a* Pressure statistics of gas nuclei in homogeneous isotropic turbulence with an application to cavitation inception. *Phys. Fluids* **32** (9), 095107.

BAPPY, M.H., VELA-MARTIN, A., BUSCAGLIA, G.C., CARRICA, P.M. & FREIRE, L.S. 2020*b* Effect of bubble size on Lagrangian pressure statistics in homogeneous isotropic turbulence. In *Journal of Physics: Conference Series*, vol. 1522, p. 012002. IOP Publishing.

BERRY, S.R., HYERS, R.W., RACZ, L.M. & ABEDIAN, B. 2005 Surface oscillations of an electromagnetically levitated droplet. *Intl J. Thermophys.* **26**, 1565–1581.

BOJAREVICS, V. & PERICLEOUS, K. 2003 Modelling electromagnetically levitated liquid droplet oscillations. *ISIJ Intl* **43** (6), 890–898.

BOUSSINESQ, J. 1877 *Essai sur la théorie des eaux courantes*. Impr. nationale.

BROUZET, C., GUINÉ, R., DALBE, M.-J., FAVIER, B., VANDENBERGHE, N., VILLERMAUX, E. & VERHILLE, G. 2021 Laboratory model for plastic fragmentation in the turbulent ocean. *Phys. Rev. Fluids* **6** (2), 024601.

CADOT, O., DOUADY, S. & COUDER, Y. 1995 Characterization of the low-pressure filaments in a three-dimensional turbulent shear flow. *Phys. Fluids* **7** (3), 630–646.

CALZAVARINI, E., VOLK, R., BOURGOIN, M., LÉVÊQUE, E., PINTON, J.-F. & TOSCHI, F. 2009 Acceleration statistics of finite-sized particles in turbulent flow: the role of faxén forces. *J. Fluid Mech.* **630**, 179–189.

CAO, N., CHEN, S. & DOOLEN, G.D. 1999 Statistics and structures of pressure in isotropic turbulence. *Phys. Fluids* **11** (8), 2235–2250.

CHANDRASEKHAR, S. 1959 The oscillations of a viscous liquid globe. *Proc. Lond. Math. Soc.* **3** (1), 141–149.

CHANDRASEKHAR, S. 2013 *Hydrodynamic and Hydromagnetic Stability*. Courier Corporation.

CHIARINI, A. & ROSTI, M.E. 2024 Finite-size inertial spherical particles in turbulence. *J. Fluid Mech.* **988**, A17.

DE LANGRE, E. 2008 Effects of wind on plants. *Annu. Rev. Fluid Mech.* **40**, 141–168.

DEIKE, L. 2022 Mass transfer at the ocean–atmosphere interface: the role of wave breaking, droplets, and bubbles. *Annu. Rev. Fluid Mech.* **54**, 191–224.

DOUADY, S., COUDER, Y. & BRACHET, M.E. 1991 Direct observation of the intermittency of intense vorticity filaments in turbulence. *Phys. Rev. Lett.* **67** (8), 983.

FAN, Y., WANG, C., JIANG, L., SUN, C. & CALZAVARINI, E. 2024 Accelerations of large inertial particles in turbulence. *Europhys. Lett.* **145** (4), 43001.

FAUVE, S., LAROCHE, C. & CASTAING, B. 1993 Pressure fluctuations in swirling turbulent flows. *J. Phys.* **3** (3), 271–278.

GALINAT, S., RISSO, F., MASBERNAT, O. & GUIRAUD, P. 2007 Dynamics of drop breakup in inhomogeneous turbulence at various volume fractions. *J. Fluid Mech.* **578**, 85–94.

GITTERMAN, M. 2005 *Noisy Oscillator, The: The First Hundred Years, From Einstein Until Now*. World Scientific.

GOTOH, T. & ROGALLO, R.S. 1999 Intermittency and scaling of pressure at small scales in forced isotropic turbulence. *J. Fluid Mech.* **396**, 257–285.

HÅKANSSON, A. 2019 Emulsion formation by homogenization: current understanding and future perspectives. *Annu. Rev. Food Sci. Technol.* **10**, 239–258.

HÅKANSSON, A. 2021 The role of stochastic time-variations in turbulent stresses when predicting drop breakup—a review of modelling approaches. *Processes* **9** (11), 1904.

HINZE, J.O. 1955 Fundamentals of the hydrodynamic mechanism of splitting in dispersion processes. *AIChE J.* **1** (3), 289–295.

HOMANN, H. & BEC, J. 2010 Finite-size effects in the dynamics of neutrally buoyant particles in turbulent flow. *J. Fluid Mech.* **651**, 81–91.

ISHIHARA, T., KANEDA, Y., YOKOKAWA, M., ITAKURA, K. & UNO, A. 2003 Spectra of energy dissipation, enstrophy and pressure by high-resolution direct numerical simulations of turbulence in a periodic box. *J. Phys. Soc. Japan* **72** (5), 983–986.

KANG, I.S. & LEAL, L.G. 1988 Small-amplitude perturbations of shape for a nearly spherical bubble in an inviscid straining flow (steady shapes and oscillatory motion). *J. Fluid Mech.* **187**, 231–266.

KOLMOGOROV, A. 1949 On the breakage of drops in a turbulent flow. In *Dokl. Akad. Navk. SSSR*, vol. 66, pp. 825–828.

KRAICHNAN, R.H. 1964 Kolmogorov's hypotheses and Eulerian turbulence theory. *Phys. Fluids* **7** (11), 1723–1734.

LALANNE, B., MASBERNAT, O. & RISSO, F. 2019 A model for drop and bubble breakup frequency based on turbulence spectra. *AIChE J.* **65** (1), 347–359.

LAMB, H. 1932 *Hydrodynamics*, vol. 427. Cambridge University Press.

LEE, C.-H., ERICKSON, L.E. & GLASGOW, L.A. 1987 Bubble breakup and coalescence in turbulent gas-liquid dispersions. *Chem. Engng Commun.* **59** (1–6), 65–84.

LUO, H. & SVENDSEN, H.F. 1996 Theoretical model for drop and bubble breakup in turbulent dispersions. *AIChE J.* **42** (5), 1225–1233.

MANIERO, R., MASBERNAT, O., CLIMENT, E. & RISSO, F. 2012 Modeling and simulation of inertial drop break-up in a turbulent pipe flow downstream of a restriction. *Intl J. Multiphase Flow* **42**, 1–8.

MARTÍNEZ-BAZÁN, C., MONTANES, J.L. & LASHERAS, J.C. 1999 On the breakup of an air bubble injected into a fully developed turbulent flow. Part 1. Breakup frequency. *J. Fluid Mech.* **401**, 157–182.

MASUK, A.U.M., QI, Y., SALIBINDLA, A.K.R. & NI, R. 2021*a* Towards a phenomenological model on the deformation and orientation dynamics of finite-sized bubbles in both quiescent and turbulent media. *J. Fluid Mech.* **920**, A4.

MASUK, A.U.M., SALIBINDLA, A.K.R. & NI, R. 2021*b* Simultaneous measurements of deforming Hinze-scale bubbles with surrounding turbulence. *J. Fluid Mech.* **910**, A21.

MAXEY, M.R. & RILEY, J.J. 1983 Equation of motion for a small rigid sphere in a nonuniform flow. *Phys. Fluids* **26** (4), 883–889.

MILLER, C.A. & SCRIVEN, L.E. 1968 The oscillations of a fluid droplet immersed in another fluid. *J. Fluid Mech.* **32** (3), 417–435.

MORDANT, N., CRAWFORD, A.M. & BODENSCHATZ, E. 2004 Three-dimensional structure of the lagrangian acceleration in turbulent flows. *Phys. Rev. Lett.* **93** (21), 214501.

NI, R. 2024 Deformation and breakup of bubbles and drops in turbulence. *Annu. Rev. Fluid Mech.* **56** (1), 319–347.

PERRARD, S., RIVIÈRE, A., MOSTERT, W. & DEIKE, L. 2021 Bubble deformation by a turbulent flow. *J. Fluid Mech.* **920**, A15.

POPE, S.B. 2000 *Turbulent Flows*. Cambridge University Press.

POPINET, S. 2003 Gerris: a tree-based adaptive solver for the incompressible euler equations in complex geometries. *J. Comput. Phys.* **190** (2), 572–600.

POPINET, S. 2009 An accurate adaptive solver for surface-tension-driven interfacial flows. *J. Comput. Phys.* **228**, 5838–5866.

PRAKASH, V.N., TAGAWA, Y., CALZAVARINI, E., MERCADO, J.M. Toschi, F., Lohse, D. & Sun, C. 2012 How gravity and size affect the acceleration statistics of bubbles in turbulence. *New J. Phys.* **14** (10), 105017.

PRANDTL, L. 1949 Report on investigation of developed turbulence. *Z. Angew. Math. Mech.* **5** (NACA-TM-1231).

PROSPERETTI, A. 1977 Viscous effects on perturbed spherical flows. *Q. Appl. Maths* **34** (4), 339–352.

PROSPERETTI, A. 1980 Free oscillations of drops and bubbles: the initial-value problem. *J. Fluid Mech.* **100** (2), 333–347.

PULLIN, D.I. & ROGALLO, R.S. 1994 Pressure and higher-order spectra for homogeneous isotropic turbulence. In *Stanford Univ., Studying Turbulence Using Numerical Simulation Databases. 5: Proceedings of the 1994 Summer Program*. https://ntrs.nasa.gov/citations/19950014628.

PUMIR, A. 1994 A numerical study of pressure fluctuations in three-dimensional, incompressible, homogeneous, isotropic turbulence. *Phys. Fluids* **6** (6), 2071–2083.

QURESHI, N.M., BOURGOIN, M., BAUDET, C., CARTELLIER, A. & GAGNE, Y. 2007 Turbulent transport of material particles: an experimental study of finite size effects. *Phys. Rev. Lett.* **99** (18), 184502.

RAVELET, F., COLIN, C. & RISSO, F. 2011 On the dynamics and breakup of a bubble rising in a turbulent flow. *Phys. Fluids* **23** (10), 103301.

RAYLEIGH, LORD 1879 On the capillary phenomena of jets. *Proc. R. Soc. Lond.* **29** (196–199), 71–97.

REID, W.H. 1960 The oscillations of a viscous liquid drop. *Q. Appl. Maths* **18** (1), 86–89.

RISSO, F. 2018 Agitation, mixing, and transfers induced by bubbles. *Annu. Rev. Fluid Mech.* **50**, 25–48.

RISSO, F. & FABRE, J. 1998 Oscillations and breakup of a bubble immersed in a turbulent field. *J. Fluid Mech.* **372**, 323–355.

RIVIÈRE, A., DUCHEMIN, L., JOSSERAND, C. & PERRARD, S. 2023 Bubble breakup reduced to a one-dimensional nonlinear oscillator. *Phys. Rev. Fluids* **8** (9), 094004.

RIVIÈRE, A., MOSTERT, W., PERRARD, S. & DEIKE, L. 2021 Sub-Hinze scale bubble production in turbulent bubble break-up. *J. Fluid Mech.* **917**, A40.

ROA, I., RENOULT, M.-C., DUMOUCHEL, C., BRÄNDLE DE MOTTA, J.C. 2023 Droplet oscillations in a turbulent flow. *Front. Phys.* **11**, 1173521.

ROSALES, C. & MENEVEAU, C. 2005 Linear forcing in numerical simulations of isotropic turbulence: physical space implementations and convergence properties. *Phys. Fluids* **17** (9), 095106.

ROSTI, M.E., BANAEI, A.A., BRANDT, L. & MAZZINO, A. 2018 Flexible fiber reveals the two-point statistical properties of turbulence. *Phys. Rev. Lett.* **121** (4), 044501.

RUTH, D.J., MOSTERT, W., PERRARD, S. & DEIKE, L. 2019 Bubble pinch-off in turbulence. *Proc. Natl Acad. Sci. USA* **116** (51), 25412–25417.

SALIBINDLA, A.K.R., MASUK, A.U.M. & NI, R. 2021 Experimental investigation of the acceleration statistics and added-mass force of deformable bubbles in intense turbulence. *J. Fluid Mech.* **912**, A50.

SEVIK, M. & PARK, S.H. 1973 The splitting of drops and bubbles by turbulent fluid flow. *Trans. ASME J. Fluids Engng* **95** (1), 53–60.

SHEN, J., PENG, C., WU, J., CHONG, K.L., LU, Z. & WANG, L.-P. 2022 Turbulence modulation by finite-size particles of different diameters and particle–fluid density ratios in homogeneous isotropic turbulence. *J. Turbul.* **23** (8), 433–453.

TENNEKES, H. 1975 Eulerian and Lagrangian time microscales in isotropic turbulence. *J. Fluid Mech.* **67** (3), 561–567.

TOSCHI, F. & BODENSCHATZ, E. 2009 Lagrangian properties of particles in turbulence. *Annu. Rev. Fluid Mech.* **41**, 375–404.

VEDULA, P. & YEUNG, P.-K. 1999 Similarity scaling of acceleration and pressure statistics in numerical simulations of isotropic turbulence. *Phys. Fluids* **11** (5), 1208–1220.

VELA-MARTÍN, A. & AVILA, M. 2021 Deformation of drops by outer eddies in turbulence. *J. Fluid Mech.* **929**, A38.

VELA-MARTÍN, A. & AVILA, M. 2022 Memoryless drop breakup in turbulence. *Sci. Adv.* **8** (50), eabp9561.

VERHILLE, G. 2022 Deformability of discs in turbulence. *J. Fluid Mech.* **933**, A3.

VOLK, R., CALZAVARINI, E., LEVEQUE, E. & PINTON, J.-F. 2011 Dynamics of inertial particles in a turbulent von Kármán flow. *J. Fluid Mech.* **668**, 223–235.

VOLK, R., CALZAVARINI, E., VERHILLE, G., LOHSE, D., MORDANT, N., PINTON, J.-F. & TOSCHI, F. 2008 Acceleration of heavy and light particles in turbulence: comparison between experiments and direct numerical simulations. *Physica* D **237** (14–17), 2084–2089.

VOTH, G.A., LA PORTA, A., CRAWFORD, A.M., ALEXANDER, J. & BODENSCHATZ, E. 2002 Measurement of particle accelerations in fully developed turbulence. *J. Fluid Mech.* **469**, 121–160.

WANG, T., WANG, J. & JIN, Y. 2003 A novel theoretical breakup kernel function for bubbles/droplets in a turbulent flow. *Chem. Engng Sci.* **58** (20), 4629–4637.

XIAO, X., BRILLO, J., LEE, J., HYERS, R.W. & MATSON, D.M. 2021 Impact of convection on the damping of an oscillating droplet during viscosity measurement using the ISS-EML facility. *npj Microgravity* **7** (1), 36.

YAO, H.-D., HE, G.-W., WANG, M. & ZHANG, X. 2008 Time correlations of pressure in isotropic turbulence. *Phys. Fluids* **20** (2), 025105.